International Journal of Hydrogen Energy 170 (2025) 151020

Contents lists available at ScienceDirect

International Journal of Hydrogen Energy

journal homepage: www.elsevier.com/locate/he

Development and validation of phenomenological models for combustion and emissions of a dual-fuel marine engine supplied with ammonia

Vincenzo De Bellis [a,1], Massimiliano De Felice [a,*,1], Enrica Malfi [a], Fabio Bozza [a], Alberto Cafari [b], Alessandro Cimarello [c], André Ahlskog [b], Viljam Grahn [b], Jari Hyvonen [b]

[a] Industrial Engineering Department, Mechanic and Energetic Section, University of Naples "Federico II", via Claudio 21, 80125, Naples, Italy
[b] Wärtsilä Finland OY, Vaasa, Finland
[c] Wärtsilä Italia S.p.A., Trieste, Italy

ARTICLE INFO

Keywords:
Ammonia
Dual-fuel engine
Phenomenological combustion model
Phenomenological emission model
Spray model

ABSTRACT

This study investigates ammonia-fueled RCCI combustion in a medium-bore research engine. Ammonia is introduced via port injection, while light fuel oil is directly injected inside the cylinder. The experimental campaign explores variations in engine load, air-to-fuel ratio, injection timing and duration, and valve timing. A phenomenological model is developed and validated, incorporating chemical kinetics and flame propagation. The framework employs a multi-zone approach to calculate fuel distribution, integrating a spray model, a tabulated method for ignition prediction, and an emissions model to estimate CO, NO, uHC, uNH_3, and N_2O concentrations. The model accurately simulates experimental results, achieving an average error below 10 % in global performance predictions and of about 20 % in pollutant emission evaluations. By capturing the key physics of RCCI combustion, this study provides valuable insights into ammonia potential as a marine zero-carbon fuel and supports the development of predictive tools for engine design and optimization.

1. Introduction

Global efforts to address the challenges of climate change necessitate the development and implementation of low-carbon processes across all energy consumption sectors. Rapid advancements in propulsion system technologies [1] are critical to achieve significant decarbonization and limit global temperature increases to 1.5 °C [2,3]. While electrification and hybridization offer viable solutions for the light-duty road transport sector [4], alternative approaches have to be pursued for hard-to-electrify domains such as aviation, off-road vehicles, and the maritime industry.

The marine transportation sector faces considerable obstacles in reducing its environmental footprint. The International Maritime Organization (IMO) has set ambitious targets to cut greenhouse gas (GHG) emissions by 50 % by 2050 compared to 2008 levels [5], with intermediate goals of a 40 % reduction in CO_2 emissions by 2030 and a 70 % reduction by 2050 [6]. In response to these objectives, the European Union (EU) has incorporated the maritime sector into its Emissions Trading System, aiming for a 55 % reduction in GHG emissions by 2030 relative to 1990 levels.

To meet these targets, the Institute of Electrical and Electronics Engineers (IEEE) estimates that 50 % of marine engines have to be adapted to zero-carbon and low-carbon fuels by the mid-2040s [7]. Given the long service life of marine engines, the adoption of these fuels is expected to make a fundamental contribution to the future of shipping in order to comply with the emissions reduction targets and ensure sustainable shipping operations. Therefore, both retrofit solutions and the development of new engine technologies are essential to decarbonize the marine industry.

A variety of zero-carbon and low-carbon fuels are being explored for commercial application in the maritime sector, including hydrogen, ammonia, natural gas (NG), and methanol [8–11]. The adoption of these alternative fuels faces several challenges, such as meeting stringent safety regulations, ensuring global availability, and addressing transportability problems. Additionally, marine engines have to operate efficiently under economically viable single- or dual-fuel combustion modes, even when fuel availability varies. Ammonia (NH_3) emerged as a promising candidate for zero-carbon fuel in marine applications,

* Corresponding author.
E-mail addresses: vincenzo.debellis@unina.it (V. De Bellis), massimiliano.defelice@unina.it (M. De Felice).
[1] These authors equally contribute to this work.

https://doi.org/10.1016/j.ijhydene.2025.151020
Received 7 April 2025; Received in revised form 10 July 2025; Accepted 15 August 2025
Available online 28 August 2025

offering significant potential for GHG emissions reduction. Like hydrogen, ammonia can be synthesized from various sources, including fossil fuels, biomass, or renewable energy such as wind and solar power. In particular, surplus renewable electricity can be converted into ammonia, serving as an efficient energy storage medium [12].

In recent years, ammonia earned increasing attention due to its potential benefits, supported by initiatives from governments (e.g. Japan [13,14], United States [15,16], United Kingdom [17,18], Australia [19], European Union [20,21]) and industry leaders [22]. Key advantages of ammonia include its low cost per unit of stored energy, high volumetric energy density, widespread production capabilities, established handling and distribution infrastructure, and commercial viability. Ammonia derived from renewable sources exhibits several useful properties:

- It is inherently carbon-free, has no direct greenhouse gas emissions, and can be synthesized through fully renewable, carbon-neutral processes.
- With a lower heating value of 18.6 MJ/kg, it offers a level of performance comparable to conventional fossil fuels.
- Ammonia can be easily liquefied under moderate conditions, requiring compression to just 0.8 MPa at ambient temperature.
- A robust and well-established infrastructure for ammonia storage and distribution already exists, encompassing pipelines, rail transport, road networks, and shipping.

Despite these advantages, ammonia poses several challenges as an engine fuel. Its toxic and flammable nature introduces specific storage and handling requirements. Furthermore, ammonia combustion characteristics present technical difficulties, including high resistance to autoignition, a high minimum ignition energy, and a low laminar flame speed, which can complicate its application in marine engines. Another critical aspect of ammonia combustion is nitrous oxide (N_2O) production. This species is a product of ammonia incomplete combustion [23] and gained a particular focus in ammonia combustion [24–27] since its high global warming potential, 273 times greater than CO_2 on a 100-years scale [28]. These drawbacks necessitate further research and technological advancements to fully realize ammonia potential as a sustainable marine fuel.

In the maritime sector, most international ship engines are large, low-speed, two-stroke compression-ignition engines that are less impacted by ammonia slow combustion velocity during ignition. However, for high-speed, four-stroke engines, significant improvements in NH_3 combustion initiation and duration are necessary to enhance efficiency. Generally speaking, most of zero- and low-carbon fuels are suited for pre-chamber or spark-ignition engine configurations. Several ignition system designs are already well-developed for small four-stroke engines fueled by natural gas and alcohols, with some progress being made in hydrogen-fueled systems and ammonia-fueled engines. However, these engines often fail to achieve the torque targets of reference diesel engines. At high engine loads, deflagration-based combustion systems exhibit issues such as knocking. Dual-fuel combustion modes provide a viable solution by using a diesel pilot in a mixing-controlled combustion process [29–31], which allows retrofitting of existing compression-ignition engines. Many ship engines retrofitted for diesel-NG dual-fuel operation, where diesel acts as the ignition source, can adapt to NH_3 with minor engine modifications. When replacing NG with NH_3, the engines can achieve power densities comparable to diesel while theoretically reducing GHG emissions in proportion to the gas-energy substitution ratio. However, N_2O generation has to be taken into account in order to correctly evaluate GHG reduction in NH_3-diesel combustion. In order to clarify the impact of ammonia substitution and N_2O production, Fig. 1 displays the GWP reduction of NH_3-diesel dual-fuel combustion with respect to pure diesel combustion, considering N_2O emissions. The GWP calculation is performed considering the CO_2-equivalent mass for each condition in the hypothesis of constant

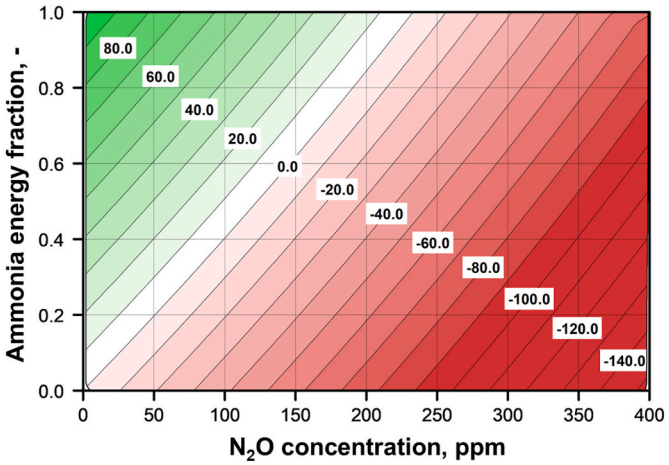

Fig. 1. GWP reduction in ammonia-diesel combustion compared to pure diesel experiments.

fuel energy content, complete combustion in lean conditions (λ equal to 2), and N_2O as a possible combustion product in the global reaction (more details about the assumptions and the equations adopted to calculate the GWP reduction are available in the Appendix section). As expected, the introduction of ammonia reduces GWP emissions since a smaller amount of CO_2 is generated. However, a higher N_2O concentration drastically reduces this gain, and may even worsen the engine carbon footprint if it exceeds values of about 230 ppm. For this reason, it is fundamental to achieve very reduced N_2O concentrations in ammonia-diesel combustions.

Advanced dual-fuel combustion strategies, such as reactivity-controlled compression ignition (RCCI) combustion [32], offer promising pathways for reducing GHG emissions. NH_3-diesel RCCI combustion is experimentally investigated for smaller four-stroke engines to achieve high combustion efficiency. The substantial reactivity differences between NH_3 (with its high RON) and HFO or distillate diesel fuel make RCCI and Active Combustion Control (ACC) promising approaches to mitigate GHG emissions [33]. Chiera et al. [34] demonstrated that substituting NH_3 could reduce GHG emissions by up to 80 %. Additionally, selective catalytic reduction (SCR) systems or catalytic converters [35,36] can be employed to mitigate high NO_x and N_2O emissions associated with NH_3 combustion, further supporting its viability as a marine fuel. Ref. [37] investigated NH_3-diesel RCCI combustion in a light duty single cylinder engine. The main objective of this experimental campaign is to provide data about efficiency and pollutant emissions with the lowest possible diesel energy fraction. The results showed that this strategy does not lead to minimal carbon footprint, and that the minimum footprint can be achieved with an ammonia equivalence ratio of 0.8 and a diesel energy fraction higher than the minimum acceptable. Ref. [38] investigated ammonia-diesel RCCI combustion with two injection strategies (single and double injections) with different timings. The outcomes demonstrated that an anticipated single injection reduces unburned NH_3 but increases NO_x and N_2O emissions. The adoption of the split injection strategies leads to an increase in combustion efficiency and a reduction in combustion instability, while also reducing all the pollutant species concentrations.

In addition to experimental tests, the literature analyzes the potentialities of NH_3-diesel RCCI or dual-fuel combustion through numerical models. These simulations can be categorized into two groups: 3D CFD simulations; 0D multi-zone models. These studies introduce novel methodologies to address the challenges associated with mixing and combustion when utilizing dual-fuel systems. The RCCI combustion process, in particular, involves multiple fuel combustion modes, presenting a significant challenge in accurately modeling these complex interactions. Ref. [39] performed a numerical 3D CFD simulations of

NH_3-diesel RCCI combustion, demonstrating that an increasing ammonia substitution percentage can drastically reduce NO_x concentrations while maintaining low concentration levels of CO, uHC and N_2O. Ref. [40] continued the previous study, substituting hydrogen in ammonia, demonstrating that this addition improves combustion efficiency while lowering the concentrations of CO, unburned NH_3, uHC, and N_2O. Ref. [27] analyzed different ammonia substitution fraction and diesel Start of Injection (SOI) through 3D CFD simulations of a heavy-duty cylinder. Compared to diesel combustion, ammonia introduction decreases thermal efficiency and NO_x concentration, while increasing N_2O concentration. Advancing the SOI, a partial compensation for the thermal efficiency reduction and N_2O concentration increase can be achieved.

In the context of 0D modeling, it is well established that multi-zone models are essential for accurately representing the key aspects of low-temperature combustion (LTC) regimes, such as spatial distributions of temperature and fuel and different modalities of mixture combustion [41]. The first aspect is critical for RCCI combustion due to its sensitivity to fuel distribution. Two primary methodologies are employed to address this challenge: assigning a predefined fuel distribution, either derived from 3D CFD simulation results or defined through tunable profiles [42], or utilizing detailed fuel spray models to capture the spatial variations [43–45]. In combustion modeling, fuel ignition is widely acknowledged as the primary combustion mode in LTC. However, studies such as [46–48] have highlighted the importance of accounting for flame propagation in RCCI combustion. The simplest approach to modeling fuel ignition involves using ignition delay correlations coupled with the resolution of the Livengood-Wu integral [49,50]. While this method offers high computational efficiency, its accuracy is limited. Alternatively, several studies [51–53] have employed detailed chemical kinetics to model fuel chemistry, providing a high level of accuracy. However, this approach significantly increases computational burden, particularly when applied to models with a large number of zones. To alleviate these challenges, researchers have explored simplified kinetic mechanisms [54] or reduced zone counts [55–57], achieving a balance between accuracy and computational effort. A more computationally efficient option involves the use of tabulated approaches to simulate ignition processes. One method is to tabulate ignition delays under various engine-relevant conditions and apply the Livengood-Wu integral [58] to determine ignition timing. While computationally rapid, this approach does not provide information on intermediate composition or temperature evolution during ignition, which can be a critical limitation, especially in scenarios involving cool flame phenomena. To address these shortcomings, an improved strategy involves tabulating the global evolution of the auto-ignition process using a progress variable, which enables a more detailed and reliable prediction of ignition behavior [42,43].

In the current literature, few works employ these kinds of models in ammonia-diesel dual-fuel and RCCI combustions. Ref. [49] utilizes a multi-zone 0D model that employs a multi-zone spray model, an ignition delay correlation to estimate the diesel ignition and a simplified flame propagation model to model the flame generated by the mixture ignition. The model is initially tuned with respect to pure diesel combustion and then tests with ammonia substitution, resulting in an acceptable prediction of heat release rate and in-cylinder pressure at different substitution percentages. Ref. [50] utilizes a multi-zone 0D model to numerically test the aqueous ammonia substitution in a compression-ignition engine. The model is constituted of a simplified spray model to compute diesel distribution, an ignition delay correlation and different correlation for the mixture combustion on the basis of the different combustion phases. Additionally, NO_x and soot are calculated with simplified models. From a modeling perspective, previous researches present several shortcomings. Fuel ignition is often over-simplified, and flame propagation is addressed in only one study, using a simplified methodology. Experimental validation is either minimal or entirely absent, and gaseous pollutant predictions are restricted to NO_x emissions.

To address these gaps, this study focuses on the development of a multi-zone 0D model, extensively validated for combustion performance and pollutant emissions, which can serve as a reliable tool for engine design and calibration. Initially designed for NG-diesel RCCI engines [43], the model has been adapted to simulate NH_3-diesel RCCI engines. It incorporates a suite of sub-models categorized as follows:

- Zonal interaction and evolution models: these include sub-models for heat transfer, diffusion, spray dynamics, and fuel evaporation, defining the inhomogeneities in the combustion chamber.
- Combustion models: these comprise an ignition model, which employs a tabulated approach (Tabulated Kinetics of Ignition), and a flame propagation model, which adopts the fractal theory.
- Emission models: these involve an unburned fuel model, a pollutant burned-zone model, and a partial oxidation model.

The novelty of the proposed phenomenological framework does not ground on specific aspects, which in their essence are taken from the literature or previous works of the authors such as, for instance, auto-ignition, spray evolution, droplet evaporation, flame propagation, but in the way they are combined and customized to describe combustion and emissions in an engine operated in RCCI mode and supplied with ammonia. In the authors' knowledge, literature is poor of phenomenological models for this kind of engine supplied with ammonia and the works in Refs. [49,50] are the only available attempts, although these present important limitations, as detailed above. Additional novelties in the presented work are:

- The verification of the adopted blending rule for the estimation of the laminar flame speed for ammonia/diesel blends through the comparison with 1D planar flame chemical kinetics calculations.
- The proposal of a one-step reaction mechanism for the evaluation of post-oxidation of ammonia.

The structure of the paper is as follows: first, the experimental setups, including the engine and constant volume spray chamber, together with the corresponding test matrices, are described; next, a detailed explanation of the 0D model and its constituent sub-models is provided; finally, the calibration and validation of the model are presented, focusing on global engine performance, exhaust pollutant concentrations, and detailed results.

2. Objects and methods

2.1. Engine description and experimental setup

The experimental campaign was conducted utilizing a marine-derived single cylinder engine (SCE), built for research scopes and adapted for operation with ammonia. The principal characteristics of the engine are collected in Table 1. The intake line is equipped with a volumetric compressor and an intercooler for an accurate control of the boost pressure and intake temperature. A throttle valve is installed in the exhaust line for the backpressure regulation, in order to simulate the

Table 1
Principal engine and sub-system characteristics.

	Specification
Bore, mm	250
Stroke, mm	340
Nominal Speed, rpm	900
Air System	External air compressor with air temperature and pressure control
Fuel System	Common rail with twin needles and ammonia admission valve
Valve train System	Fully flexible

Table 2
Experimental SCE test matrix.

Case	Sweep Label	Load [%]	Δλ [−]	$\Delta\theta_{Inj}$ [CAD]	Norm. τ_{Inj} [−]	$\Delta\theta_{IVC}$ [CAD]	Norm. y_{LFO} [−]
1	$\Delta\theta_{IVC}$	25	0.0	−20	0.69	66	1.83
2	LL	25	0.0	−20	0.69	56	1.86
3		25	0.0	−20	0.69	47	1.87
4	Δλ LL	25	−0.1	−20	0.71	56	1.97
5		25	−0.1	−14	0.69	57	1.86
6		25	0.1	−20	0.71	56	2.03
7		25	0.3	−20	0.71	56	1.92
8		25	0.4	−20	0.69	57	1.89
9		25	0.7	−20	0.69	56	1.93
10	τ_{Inj} LL	25	0.2	−20	0.68	57	1.73
11		25	0.2	−20	0.70	57	1.89
12		25	0.1	−20	0.72	57	2.11
13	Δλ HL	85	−0.1	−26	0.81	15	1.32
14		85	0.0	−26	0.81	15	1.34
15	$\Delta\theta_{Inj}$ HL	85	−0.1	−20	0.81	15	1.39
16		85	−0.1	−26	0.81	15	1.34
17	Load	10	0.0	−15	0.63	71	1.97
18		25	0.0	−10	0.66	61	1.59
19		50	0.0	−5	0.69	47	1.17
20		75	0.0	0	0.81	6	1.18
21		90	0.0	0	1.00	0	1.00

typical conditions of a turbocharged engine. The main fuel, ammonia, is injected in vapor phase into the intake line through a low-pressure solenoid valve. A high-pressure common rail injection system is employed for the light fuel oil (LFO) direct injector, in order to ease the air-fuel mixture.

The main goal of the experimental campaign is the assessment of the capabilities and limitations of an ammonia-fueled marine engine. In this perspective, the experimental campaign is subdivided into three main blocks. The first one, consisting of 12 operating conditions, is designed fixing a low load condition (25 %) and performing sweeps of relative intake valve closure ($\Delta\theta_{IVC}$), relative air-to-fuel ratio (Δλ), and normalized injection duration (τ_{Inj}). The second block, consisting of 4 operating conditions, is designed fixing a high load condition (85 %) and performing sweeps of relative air-to-fuel ratio (Δλ), and relative injection timing ($\Delta\theta_{Inj}$). To conclude, the last 5 operating conditions represent a load sweep with optimized engine parameters. In order to stabilize the combustion process, the proportion between LFO and ammonia, defined as y_{LFO} in Eq. (1), is optimized for each operating condition.

$$y_{LFO} = \frac{m_{LFO} LHV_{LFO}}{m_{LFO} LHV_{LFO} + m_{NH3} LHV_{NH3}} \quad (1)$$

Table 2 provides details about the operating conditions of the test matrix. To preserve confidentiality, the parameters are normalized with respect to Case #21. Some of them (Δλ, $\Delta\theta_{Inj}$, $\Delta\theta_{IVC}$) are defined as differences with respect to the reference case (e.g. $\Delta\lambda = \lambda - \lambda_{ref}$), while the normalized τ_{Inj} and y_{LFO} are defined as the ratio between the current and reference values.

During engine operation, different global values are measured (LFO and ammonia consumptions, air flow rate, wall temperatures and exhaust gases concentrations), in combination with the in-cylinder instantaneous pressure. For the global parameters, the test procedure entails that the acquisition time for global values covers 3 min with a sample rate of 10 Hz, and then the time-average values are extracted. For the in-cylinder pressure, the signal is recorded for 300 consecutive cycles with a 0.2 CAD resolution. The stability of the engine operation is guaranteed by the verification that the IMEP CoV is lower than 2.5 % in all tested operating conditions. Although the above procedure does not provide quantitative metrics about repeatability of the experiments and of the measurement noise, the indicated analysis can be considered adequately reliable thanks to the "ensemble average" process over a large number of cycles and the same applies for the global data thanks to a long acquisition time and to the stability of the combustion during this time. Table 3 provides information about the instrument accuracies employed in the experiments.

2.2. Constant volume spray chamber setup

The experimental campaign also included an investigation on the spray characteristics generated by the LFO fuel injection. The main goal of this activity is to characterize the spray behavior in terms of cone angle and tip penetration, in order to properly calibrate the spray model available in the simulation framework. The injector used in these experiments matches the one installed in the SCE, and the principal characteristics of the latter are listed in Table 4.

The spray chamber employed in this study is cubic, and it is constructed with a circular window in the upper part, having a diameter of 180 mm (Fig. 2). At the bottom side of the chamber the injector is installed in centered position. A high-speed imaging system is utilized to capture the spray evolution, with the camera placed on the upper side of the chamber, surrounded by four LED lights, as depicted in Fig. 2. Four lights are used to uniformly illuminate the chamber and enable the use of short exposure times to freeze the motion of the spray. The measurement principle adopted in the spray tests is the elastic scattering of light from the droplets in the spray. This methodology allows to measure the morphological characteristics (cone angle, tip penetration) of all the spray plumes positioning the camera in front of the injector, as detailed in Ref. [59].

Considering the centered location of the injector and the umbrella angle of the injector nozzles (Table 4), the maximum visible path length of the spray plumes is about 100 mm. The ambient conditions for the spray evolution are accurately controlled acting on the thermodynamic parameters of the mixture trapped in the spray chamber. In particular, the desired chamber pressure is obtained through a compressor, while the temperature is controlled with the chamber body warming. The spray chamber dataset is formed by 6 sweeps of injection duration with different chamber pressures and injection pressures. The injection duration spans from 700 to 1200 μs, with a step of 50 μs. The mixture temperature is set to 300 K in order to purposely avoid ignition inside the chamber. The spray chamber test matrix is listed in Table 5.

The images recorded with the high-speed camera during the spray evolution are read with a Matlab image post-processing toolbox and then processed and analyzed with a specifically developed tool in order to extract the main spray characteristics. The measurements of each plume are then combined in order to derive an average spray evolution.

Table 3
Engine experimental equipment.

Parameter	Instrument	Uncertainty
Pressure	Kistler transducer	0.2 %
Air flow rate	Coriolis type flowmeter	0.35 %
Ammonia flow rate	Coriolis type flowmeter	0.35 %
Light fuel oil flow rate	Gravimetric balance	0.2 %
In-cylinder wall temperatures	Type K Pentronic thermocouple	1.5 °C
Exhaust species concentration	Horiba Mexa-One (CO, NO, uHC, uNH_3, N_2O)	1 %

Table 4
Injector characteristics.

Specification	Value
Nozzle diameter	384 μm
Umbrella angle ($\theta_{umbrella}$)	140°

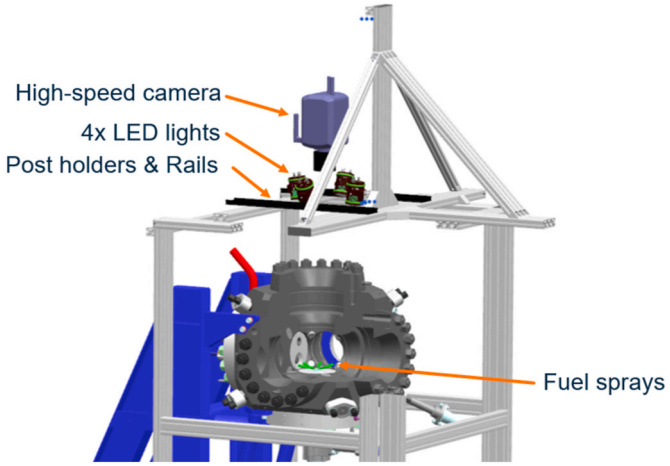

Fig. 2. Constant volume spray chamber setup.

Table 5
Experimental spray chamber test matrix.

Test Case	Chamber Temperature [K]	Chamber Pressure [bar]	Injection Pressure [bar]	Injection Duration [μs]
T1	300	5	2200	700:50:1200
T2	300	15	2200	700:50:1200
T3	300	25	2200	700:50:1200
T4	300	35	2200	700:50:1200
T5	300	5	1400	700:50:1200
T6	300	15	1400	700:50:1200

2.3. Engine model

The employment of more fuels with differing physical and chemical characteristics significantly complicates the combustion evolution, presenting relevant challenges for its modeling in a 0D model. This model needs to describe a variety of interdependent phenomena, such as air-fuel mixing, auto-ignition, and flame propagation. Research indicates that the initial auto-ignition is primarily related to the high-reactivity fuel (HRF), while low-reactivity fuel (LRF) governs flame propagation and/or delayed auto-ignition [60]. Given the critical role of HRF auto-ignition chemistry in dual-fuel combustion, accurately capturing its local reactivity is a fundamental requirement for an RCCI model. Therefore, local reactivity is highly sensitive to the local proportion between air, HRF and LRF, requiring precise tracking of HRF distribution inside the cylinder.

The HRF in-cylinder distribution may be predicted through various approaches, such as implementing a specialized spray model [61,62], utilizing experimental outcomes obtained from spray experiments, or utilizing CFD outcomes [63]. Another option involves assigning a predefined fuel distribution in the cylinder, which can be modified by adjusting specific tuning parameters [64]. The authors successfully implemented in the model a predefined distribution [42] and a dedicated spray model [43] in distinct activities, demonstrating the better versatility and the general improvements of the adoption of the spray model in the 0D model.

The model presented here aims to capture the essential physical phenomena characteristic of RCCI engines, such as the distribution of injected fuel in the combustion chamber, heat and mass flows inside the cylinder, and the fuel combustion via auto-ignition and/or flame propagation processes [46,65–67]. Leveraging the custom coding functionality of commercial software, the model has been implemented. In each simulated engine cycle, the model calculates the initial in-cylinder thermodynamic conditions and composition at intake valve closure (IVC) through a 1D intake and exhaust systems flow model. The upcoming section will describe the 0D in-cylinder model framework in terms of zone structure and balance equations. Subsequently, the sub-models that compose the framework will be detailed. In particular, the sub-models are categorized in: zonal interaction and evolution models, including the heat transfer model, the diffusion model, the spray model and the evaporation model; combustion model, encompassing the ignition model and the flame propagation model; the emission model, comprising the unburned fuel model, the pollutant burned zone model and the partial oxidation model.

2.3.1. 0D in-cylinder model

In this model framework, two zonal division structures are combined: an axisymmetric and cylindrically shaped zonal structure for capturing the combustion chamber gradients, and conical shaped volumes to represent the spray plumes generated by a multi-hole injector. As a result, the in-cylinder zones are classified into two types: “in-spray zones”, formed by the intersection of the spray volumes with the cylindrical discretization, and “out-spray zones”, that include the remaining volumes outside the spray intersections. Fig. 3 provides a visual depiction of this zone classification.

In Fig. 3, the “in-spray” zones, represented by sky blue-shaded sectors, are formed by the intersection of spray volumes with the cylindrical zones, while the orange-shaded regions correspond to the “out-spray” zones. The proposed approach assumes symmetry in the circumferential direction, thereby neglecting potential asymmetries. However, it incorporates radial stratifications of composition and thermodynamic

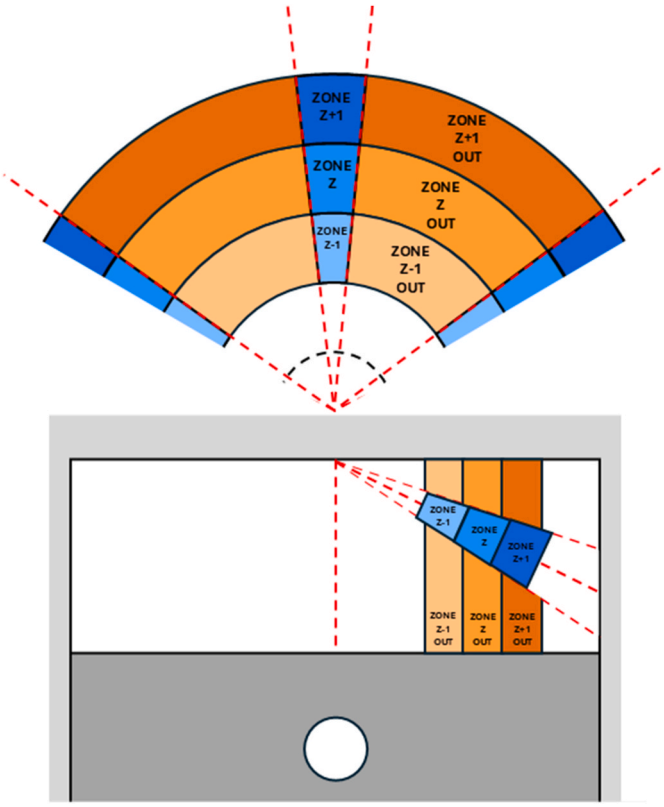

Fig. 3. Cylinder zone structure schematization, top and lateral views.

states, distinguishing between zones located inside and outside the spray regions. Each generic zone, denoted as *z*, is encircled by the adjacent zones *z+1*and *z–1*, as well as the corresponding in-spray or out-spray zone, labelled as *zOUT*.

Based on the conditions determined by the 1D intake and exhaust systems flow solver, the thermodynamic state and composition of the in-cylinder zones are defined at the start of each engine cycle, corresponding to the IVC. At this step, the cylinder mass is evenly allocated between the zones, with the assumption of a uniform mixture of air, ammonia, and residual species, together with a consistent thermodynamic state. The differentiation between in-spray and out-spray zones begins at the start of injection, when the volume corresponding to the spray plumes is calculated and subtracted from the cylindrical zones. Inside the spray regions, an initial uniform distribution of pressure, temperature, and gas composition is imposed, with mass allocated based on uniform density.

The governing equations for each zone are derived under the following hypotheses:

- The combustion chamber mixture behaves as an ideal gas.
- Pressure is equal in all the zones.
- The unburned gas is divided into multiple zones, with auto-ignition modeled using tabulated chemical kinetics.
- The burned gas is represented as a single zone, with its composition assumed to be at chemical equilibrium.

For the unburned zones, two balance equations are solved to determine temperature and composition evolution. Species composition for species *i-th* in the zone *z-th* is calculated using a species balance equation, which is generally expressed in Eq. (2).

$$\frac{dm_{i,z}}{dt} = \frac{dm_{i,AI,z}}{dt} + \frac{dm_{i,evap,z}}{dt} + \dot{m}_{i,inj,z} + \dot{m}_{i,z,z\pm1} + \dot{m}_{i,z,zOUT} - \dot{m}_{i,b,z} \tag{2}$$

In this equation, $dm_{i,AI,z}/dt$ represents the species variation rate due to chemical kinetic evolution for auto-ignition, the term $dm_{i,evap,z}/dt$ accounts for the liquid fuel evaporation, the term $\dot{m}_{i,inj,z}$ denotes the injected fuel mass flow rate, which is applied only for the first in-spray zone located on the cylinder axis, while is zero in all other zones, the term $\dot{m}_{i,z,z\pm1}$ describes the species flows between the encircled zones of the same type, while $\dot{m}_{i,z,zOUT}$ represents the species flows between the paired in-spray/out-spray zones. Additionally, $\dot{m}_{i,b,z}$ corresponds to the species flow rate evolving from the unburned zones to the burned zone. The global burning rate, the computation of which will be detailed in a subsequent section, is allocated between the unburned zones based on their respective mass fractions.

The second equation is an energy balance equation, whose general form is provided in Eq. (3):

$$\frac{dE_z}{dt} = \begin{cases} -p\frac{dV_z}{dt} - \frac{\delta Q_{W,z}}{dt} - \frac{\delta Q_{evap,z}}{dt} + \dot{m}_{inj,z}h_{inj} + \dot{Q}_{z,z\pm1} + \dot{Q}_{z,zOUT} + \\ + \sum_{i=1}^{N_{spc}} \dot{m}_{i,z,z\pm1}h_{i,z,z\pm1} + \sum_{i=1}^{N_{spc}} \dot{m}_{i,z,zOUT}h_{i,z,zOUT} - \dot{m}_{b,z}h_{u,z} \end{cases} \tag{3}$$

In this equation, E_z indicates the total internal energy, while the term pdV_z/dt accounts for the work due to piston motion and to the expansion or contraction of neighboring zones. The heat transfer rate to the cylinder walls in contact with the zones is denoted by $\delta Q_{W,z}/dt$, whereas $\delta Q_{evap,z}/dt$ represents the heat absorbed from the fuel evaporation, that is subtracted to the cylinder walls. The term $\dot{m}_{inj,z}h_{inj}$ represents the enthalpy flow due to fuel injection. The terms $\dot{Q}_{z,z\pm1} + \dot{Q}_{z,zOUT}$ represents the diffusive heat exchanges between the zones, while the terms $\dot{m}_{i,z,z\pm1}\ h_{i,z,z\pm1} + \dot{m}_{i,z,zOUT}\ h_{i,z,zOUT}$ denotes the mass flows of species and their associated enthalpies. The interzonal flow enthalpies, $h_{i,z,z\pm1}$ and $h_{i,z,zOUT}$, are evaluated with an upwind approach. The final term in Eq. (3) indicates the enthalpy flow from each unburned zone to the burned region. From Eq. (2) and Eq. (3), the temperature derivate equation can be derived, as expressed in Ref. [43].

In a similar way to the unburned zones, the species and energy balance equations are solved for the burned zone. The species balance equation is reported as Eq. (4):

$$\frac{dm_{i,b}}{dt} = \frac{dm_{i,chem,z}}{dt} + \sum_{z=1}^{N_z} \dot{m}_{i,b,z} \tag{4}$$

This equation follows a similar form with Eq. (2), where the term $dm_{i,chem,b}/dt$ represents the change in species associated with the evolution of equilibrium gas composition, along with the contribution of the species flows from the unburned regions. Likewise, in alignment with Eq. (3), an energy balance equation is formulated, considering work due to piston motions, heat transfer to the walls, and convective flow from the unburned zones. This equation is reported as Eq. (5):

$$\frac{dE_b}{dt} = -p\frac{dV_b}{dt} - \frac{\delta Q_{W,b}}{dt} + \sum_{z=1}^{N_z} \dot{m}_{b,z}h_{u,z} \tag{5}$$

Again, rearranging Eq. (4) and Eq. (5), it is possible to obtain the burned zone temperature time derivative equation. To evaluate the time evolution of the thermodynamic state and to couple the zones, the time derivative of pressure is also calculated by differentiating the ideal gas state equation and integrating it alongside the energy balances for both the unburned and burned zones.

After the description of the general equations solved in the 0D cylinder model, the description of all the sub-model integrated in the framework for the characterization of the different equation terms will be presented.

2.3.2. Zonal interaction and evolution models

In this section, the mechanisms of interaction between the zones, interaction between zones and cylinder walls, and the variation of the zonal composition not addressable to combustion phenomena will be discussed. Starting from the interactions between the zones, the generical terms can be expressed as:

$$\dot{m}_{i,z,z\pm1} = \dot{m}^{diff}_{i,z,z-1} + \dot{m}^{diff}_{i,z,z+1} + \dot{m}^{spray}_{i,z,z-1} - \dot{m}^{spray}_{i,z,z+1} \tag{6}$$

$$\dot{m}_{i,z,zOUT} = \dot{m}^{diff}_{i,z,zOUT} + \dot{m}^{spray}_{i,z,zOUT} \tag{7}$$

$$\dot{Q}_{z,z\pm1} + \dot{Q}_{z,zOUT} = \dot{Q}^{diff}_{z,z-1} + \dot{Q}^{diff}_{z,z+1} + \dot{Q}^{diff}_{z,zOUT} \tag{8}$$

The first two terms of Eq. (6) and the first term of Eq. (7) correspond to mass diffusion mechanism between the zones, driven by species concentrations gradients across adjacent zones. These terms are calculated according to Eq. (9):

$$\begin{aligned} \dot{m}^{diff}_{i,z,z-1} &= A_{z,z-1}\lambda_t k_{diff,m}\left(\frac{\Delta x_i}{\Delta r}\right)_{z,z-1} \\ \dot{m}^{diff}_{i,z,z+1} &= A_{z,z+1}\lambda_t k_{diff,m}\left(\frac{\Delta x_i}{\Delta r}\right)_{z,z+1} \\ \dot{m}^{diff}_{i,z,zOUT} &= A_{z,zOUT}\lambda_t k_{diff,m}\left(\frac{\Delta x_i}{\Delta r}\right)_{z,zOUT} \end{aligned} \tag{9}$$

In these expressions, $A_{z,z+1}$, $A_{z,z-1}$, $A_{z,zOUT}$ represent the contact areas between zones *z* and *z+1*, *z-1*, in-spray/out-spray, respectively. The parameter Δr denotes the centerline distances of surrounding zones, Δx_i represents the relative mass fraction difference, and λ_t is the total (including both turbulent and laminar effects) conductivity, calculated using the methodology described in Ref. [68]. A tuning constant, $k_{diff,m}$, is applied to adjust this equivalent conductivity. The terms in Eq. (8) describe the heat diffusion between the zones. They are calculated in a similar way to Eq. (9). However, in this case, the concentration difference is replaced by the temperature difference, and a separate tuning constant, $k_{diff,q}$, is used for adjustments.

The last two terms in Eq. (6) and the last term in Eq. (7) correspond to the mass transport associated with spray evolution. The spray model adopted in this study builds upon the approach proposed in Ref. [62] and improved with some modifications, utilizing a control volume methodology that extends from the injector nozzle to the cylinder walls. This control volume is defined by a conical geometry, characterized by a specified spray cone angle. The volume is subdivided into smaller segments, and balance equations for fuel mass and momentum along the spray axis are solved for each segment. These equations enable the calculation of spray penetration in the control volume and the temporal evolution of the spray composition, considering the relative proportions of fuel and air. To simplify the modeling approach, some hypotheses are made: the spray angle remains constant, and radial distribution is assumed to be unchanging. During the injection phase, this model has been shown to yield results consistent with the steady-jet solution [69], while also accounting for the effects of the entrainment wave following the end of injection (EOI) [70], which is a critical phenomenon in the late-stage evolution of the spray. As extensively discussed in the literature, the key parameters influencing spray temporal evolution in terms of penetration and volume occupation include ambient and fuel densities, injection pressure and duration, as well as the geometric characteristics of the injector, particularly the hole diameter. To capture these dependencies, specific input data are required for the spray jet model. For defining the control volume, the nozzle diameter and spray cone angle are essential. The instantaneous cone angle for each test was determined by post-processing experimental data, and a representative cone angle value was derived for each test using an averaging method. These results were subsequently compiled to establish a correlation for the cone angle as a function of the most significant parameters [71–74]. Consistent with the findings in Ref. [74], the parameters most affecting the spray cone angle were identified as the ambient density (ρ_a) and the injected fuel density (ρ_{fuel}), as expressed in Eq. (10):

$$\vartheta_{cone} = 4.204 \cdot atan\left(369.218\left(\frac{\rho_a}{\rho_{fuel}}\right)^{1.396}\right) + 12.1 \tag{10}$$

The developed correlation, combined with an appropriate mathematical framework, ensures that the spray jet model accurately responds to variations in ambient and fuel densities in a physically consistent manner. Another critical input required for the model is the fuel injection profile. In this activity, a symmetrical trapezoidal profile is developed and employed in the model. The key features of the profile are represented in Fig. 4.

For the characterization of the injection profile, it is mandatory to define the total duration of the profile, the temporal duration of the two ramps (in this case, it is assumed the same duration for both the increasing and decreasing ramp) and the maximum mass flow rate. For the latter, the value is derived using the incompressible flow equation

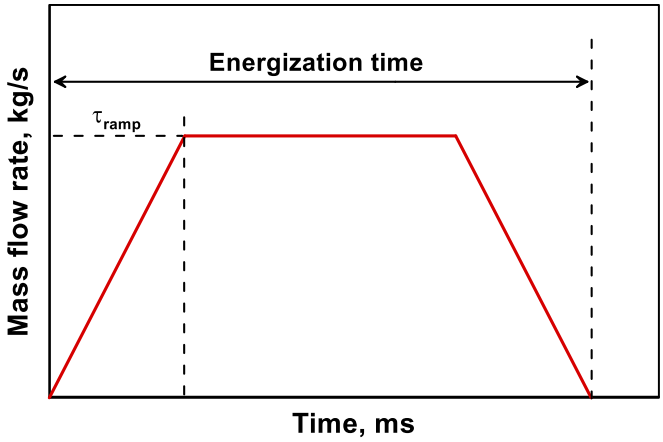

Fig. 4. Reference injection profile.

for fluid passage through an orifice, given the injection pressure and the nozzle characteristics (including the number of holes, their diameters, and the flow discharge coefficient). The profile duration is set equal to the energizing duration, while the ramp duration and the discharge coefficient are derived from the experiments at different injection pressures and rearranged in simplified correlations, reported in Eq. (11).

$$\begin{aligned} c_D &= 3.75{\cdot}10^{-5}\left(p_{Inj} - 1400\right) + 0.5 \\ \tau_{ramp} &= -2.5{\cdot}10^{-5}\left(p_{Inj} - 1400\right) + 0.1 \end{aligned} \tag{11}$$

In this equation, c_D represents the discharge coefficient, τ_{ramp} indicates the ramp time duration in milliseconds, and p_{Inj} symbolizes the injection pressure in bar. This methodology allows the model to incorporate the effects of the injector's key geometric features, as well as the injection pressure and duration, thereby enhancing its predictive capability.

Although the adopted spray model may not fully reflect transient injection effects, some aspects are taken into account, such as:

- Injection law is trapezoidal, and hence leads, during the injection tail, to slower local speeds and bigger droplets.
- As soon as the injection ends, the spray momentum is no longer fed at the tail of the column. This generates the so-called "entrainment wave" that suddenly increases the mixing of the injected fuel from the tail to the head, leading to typical fuel-lean regions close to the injector and resulting in triangular fuel distribution and speed profiles along the jet axis after the EOI.

In addition to the approach of [62], the spray model implemented in this framework is improved with the integration of the near-wall spray expansion mechanism [75], as described in the previous work of the authors [43]. This phenomenon is mathematically represented by the last term in Eq. (7) and calculated according to Eq. (12):

$$\dot{m}^{spray}_{z,zOUT} = \dot{m}^{spray}_{z,z-1} k_{out,spray}\left(\frac{s - s_0}{1 - s_0}\right) \tag{12}$$

The fuel flow exiting from the zone z, $\dot{m}^{spray}_{z,zOUT}$, is assumed to be proportionally related to the mass flow entering from the preceding in-spray zone, z-1, modulated by a constant, $k_{out,spray}$, and a non-dimensional weighting factor that accounts for the relative position along the spray axis. In this formulation, s represents the generic relative position of the zone along the spray axis, while s_0 represents the initial position where the expansion begins (treated as a tuning parameter). This term is calculated only when it yields positive values, meaning it applies solely to zones where $s > s_0$.

The liquid fuel evaporation is described utilizing the droplet evaporation model developed in Ref. [76]. This model calculates the evaporation of a single moving droplet in evaporating conditions solving the energy and mass balance equations. The main hypotheses of the model are the following:

- Quasi-steady conditions for the gas phase mass and its heat transfer.
- Negligible pressure drop in the gas phase.
- Employment of the "film theory" for boundary conditions (boundary conditions applied to a finite distance).
- Uniform fuel vapor concentration distribution at the droplet surface.
- Uniform temperature distribution in the droplet (surface included).

In accordance with the hypotheses listed above, the energy balance, rearranged to estimate the temperature derivative, is reported as Eq. (13):

$$m_{drop} c_{Fuel} \frac{dT_{drop}}{dt} = \begin{cases} \pi \bar{k}_g d_{drop} Nu^* \dfrac{\ln(1 + B_T)}{B_T}\left(T_u - T_{drop}\right) + \\ -\Delta H_{vap} \dfrac{dm_{drop}}{dt} \end{cases} \tag{13}$$

In this equation, T_{drop} represents the droplet temperature, m_{drop} denotes the droplet mass, c_{fuel} symbolizes the heat capacity of the liquid fuel, $\overline{k}_g$ indicates the average thermal conductivity, d_{drop} is the droplet diameter, Nu^* denotes the corrected Nusselt number, B_T indicates the thermal Spalding number, T_u symbolizes the unburned gas temperature, and ΔH_{vap} represents the heat of vaporization. The equation presents two competitive terms: the first one, that represents the convective heat transfer with the surrounding ambient, generally leads to the droplet temperature increase if the unburned temperature is higher; the second term, that represents the heat loss due to evaporation, leads to a temperature reduction. The second equation to be solved is the droplet mass balance equation, that is expressed in two forms on the basis of the droplet temperature:

$$\frac{dm_{drop}}{dt} = \begin{cases} \pi \overline{\rho}_g \overline{D}_g d_{drop} Sh^* \ln(1+B_M) & p_{sat}(T_{drop}) < p_{cyl} \\ \pi \dfrac{\overline{k}_g}{\overline{c}_{p,fuel}} d_{drop} Nu^* \ln(1+B_T) & p_{sat}(T_{drop}) = p_{cyl} \end{cases} \quad (14)$$

The first form of the equation is applied if the saturation pressure (p_{sat}) at the droplet temperature is lower than the ambient pressure (p_{cyl}), meaning that the droplet is not in boiling conditions, and the mass diffusion is the leading phenomenon, while the second form is applied when the droplet is in boiling condition and the heat diffusion is predominant. In this equation, $\overline{\rho}_g$ denotes the average fuel density, $\overline{D}_g$ indicates the average mass diffusivity, Sh^* symbolizes the corrected Sherwood number, B_M is the mass Spalding number, and $\overline{c}_{p,fuel}$ represents the average specific heat capacity at constant pressure. Note that the properties, denoted with symbol "$\overline{\ }$", correspond to an average between properties on the surface of each droplet and properties far from those, adopting as weighing method the linear rule proposed in Ref. [77].

The initial droplet diameter at the injector holes is determined based on the correlation outlined in Ref. [78]. As known, the initial droplet sizing has a great influence on the injected fuel evaporation rate. Anyway, in all considered operating conditions for the investigated engine, the injection occurs very early during the compression stroke, and hence the fuel evaporates quite before TDC, even introducing relevant modifications (±20 %) to the prediction of the adopted correlation for droplet size initialization. This aspect would have had a critical effect on the combustion prediction in case of injections later those here considered, where injected fuel just acts as a "liquid spark plug" and the injection timing is used as a trigger for flame propagation onset. This is not the case of the analyzed injection timings, that are well before the TDC.

In this model, LFO is represented as n-dodecane, with its thermophysical properties adopted for the evaporation process. Leveraging data obtained from the spray model, in particular the local flow velocity and droplet distribution, the evaporation model is employed to evaluate the evolution of droplet diameters and the associated phase transition from liquid to vapor in all the in-spray zones except the last one, in which a liquid film evaporation model [79] is employed. This is based again on the solution of mass and temperature equation in the liquid layer on the cylinder surface, and it is able to sense both the wall temperature and in-cylinder flow intensity. This last information is obtained from the turbulence model, that will be detailed in the upcoming section.

The evaporated portion of the injected fuel is assumed to mix with the gases entrained in the spray cone (composed of air, residuals and ammonia), leading to a mixture at a homogeneous temperature, pressure and composition for each of the "in-spray" zones of the multi-zone model. In this way, the proposed numerical approach allows to track, not only the spray tip penetration, but also the temporal evolution along the jet axis of the liquid and vapor phases of the injected fuel.

The wall heat transfer term is calculated according to:

$$\frac{\delta Q_{W,x}}{dt} = H_t A_x (T_x - T_W) \quad (15)$$

In this equation, A_x denotes the heat transfer surface area, T_x the zone temperature, T_W is the wall temperature, and H_t refers to the convective heat transfer coefficient, which is calculated using the Woschni correlation [80]. The subscript x applies to either the *z-th* unburned zone or the burned zone. The heat transfer surface area for each unburned zone is estimated on the basis of the geometric schematization of the zones. In this setup, the inner cylindrical zones are in contact with the piston and cylinder head, while the outermost zone also interfaces with the cylinder liner. Conical zones in the spray region do not directly exchange heat with the cylinder walls, except for the outermost one. Wall surface temperatures, derived from experimental data, are treated as constants in the model.

2.3.3. Combustion models

In this section, the two combustion models, namely the ignition model and the flame propagation model, implemented in the framework and their mutual interactions will be displayed. The integration of two combustion mechanisms is necessary to improve the prediction of the model and make it more generic in adoption. As mentioned earlier, ignition represents the main mechanism in RCCI combustion, but as demonstrated in Refs. [46–48] it is also possible to find propagation combustion in RCCI combustion. The mentioned references underlined that in dual fuel engines, where one fuel (usually with lower reactivity) is premixed with the air and the other fuel (usually with higher reactivity) is directly injected in liquid form in the cylinder may lead to the coexistence of auto-ignition and chemistry controlled combustion mechanism, especially in the cylinder portion richer of HRF, and flame propagation where the LRF is predominant. In light of these considerations, proper models are implemented in the adopted simulation framework to describe the above-described fuel consumption mechanisms.

Starting from the first one, a conventional approach [81,82] can be employed to determine the rates of species formation and consumption, utilizing a chemical kinetics solver that manages the relevant reaction mechanisms. Even with a reduced set of species and reactions, the computational demands associated with solving chemistry for each time step and zone in a 0D multi-zone model can be considerable. To address this, the Tabulated Kinetics of Ignition (TKI) approach is adopted in this study, as described and validated in Refs. [42,43,83].

This method condenses the ignition process into a progress variable, with its derivative pre-tabulated for a range of initial thermochemical conditions. During the simulation, this tabulated data is used to calculate the term $dm_{i,AI,z}/dt$ specifically for the vapor phase and gaseous species in each unburned zone. By replacing hundreds or thousands of individual chemical reactions with a single progress reaction variable, the TKI approach delivers results closely approximating real-time chemistry, particularly with respect to the heat release rate, while significantly reducing computational requirements. The primary limitation of this method is its inability to track intermediate species, a factor reputed to be non-critical for the objectives of this study.

The core of the TKI approach lies in modeling heat release from the auto-ignition process, based on offline chemistry simulations conducted in an adiabatic homogeneous reactor. The reactor initial conditions are designed to reflect all plausible engine-like conditions. Critical parameters influencing chemical reactions include pressure, temperature, and the composition of reactants, characterized by the fuel/air equivalence ratio, residuals mass fraction, and mass of LFO relative to total fuel. The discretization criteria used for the tabulation of the progress variable and the access variables, such as pressure, temperature, equivalence ratio, residual ratio, fuel proportions were investigated in previous studies of the authors, and the effectiveness of these criteria was verified against results of direct real-time chemistry computation in constant volume/pressure reactors and engine operations [83–85]. Accurate representation of combustion in dual-fuel engines requires the careful selection of fuel surrogates and corresponding chemical kinetic

mechanisms. In absence of specific data, LFO is modeled as n-dodecane [86], selected as the surrogate appropriate for the engine operation in RCCI mode. This choice is very common in the spray/combustion simulation, as already done for instance in Refs. [87–89]. Auto-ignition processes for both ammonia and diesel fuel are simulated using a reduced chemical kinetic mechanism [86], which includes 176 species and 2839 reactions.

The flame propagation model estimates the flame burn rate using the principles of fractal theory [90,91], which incorporates a turbulence sub-model [92] as outlined in prior research [42,43]. This turbulence sub-model provides estimates of the average in-cylinder turbulence properties, including intensity and temporal/spatial scales. The mass of fuel burned ($\dot{m}_b$) is determined based on the following expression:

$$\dot{m}_b = \rho_u A_L S_L \frac{A_T}{A_L} = \rho_u A_L S_L \Xi \tag{16}$$

In this equation, ρ_u represents the average density of the unburned gas, A_T/A_L denotes the ratio of turbulent to laminar flame front areas, S_L symbolizes the laminar flame speed, and Ξ represents the flame wrinkling factor. The wrinkling factor is derived based on fractal geometry theory [91], that establishes a relationship between the degree of flame wrinkling and the characteristic length scales of the largest (Γ_{max}) and smallest (Γ_{min}) flame structures, along with the fractal dimension D_3, as described by the following expression:

$$\Xi = \left(\frac{\Gamma_{max}}{\Gamma_{min}}\right)^{D_3-2} \tag{17}$$

The minimum wrinkling scale is assumed to coincide with the Kolmogorov length scale of the turbulent flow field, while the maximum scale is considered proportional to the flame radius, modulated by a tuning parameter, c_{wrk}. Additionally, a tuning parameter, c_{trans}, is introduced to regulate the transition from an initial quasi-laminar burning regime, where $\Xi = 1$, to a fully developed turbulent flame propagation, and another tuning constant, c_{xwc}, is introduced to modulate the transition from the fully developed turbulent flame propagation to the wall combustion, where the propagation reverts to laminar conditions [92]. The total burning rate described in Eq. (16) is distributed across zones according to their respective mass fractions, yielding the zonal burning term $\dot{m}_{b,z}$ in Eq. (2), Eq. (3), Eq. (4) and Eq. (5). The selection of the fractal theory to describe the flame propagation mechanism grounds on its better effectiveness also in comparison to other models, as demonstrated by the authors in previous researches [93].

To improve the representation of the combustion process under ultra-lean and blended conditions, an enhanced approach to calculating the laminar flame speed is utilized. Specific laminar flame speed correlations are applied for both ammonia [94] and light fuel oil [95], with the flame propagation characteristics of LFO approximated to those of n-heptane. The overall S_L is determined by blending values from individual "pure fuel" correlations, using the mass fractions as weighting factors [96]. The reliability of this methodology is confirmed in Fig. 5 with the comparison between the "mass-average blended" S_L and the actual S_L estimated with the chemical kinetic calculations in a plug-flow reactor, employing the kinetic scheme adopted for the TKI offline calculations [86]. In this figure, the pure ammonia S_L and two blends with an energy LFO percentage of 16.7 % and 30.5 % respectively are considered.

The implementation of dual combustion mechanisms presents considerable challenges in managing the interaction between the two models. During the compression phase, even before the direct injection of the HRF, only auto-ignition mechanism is enabled for the combustion heat release. As expected, the injection of a liquid and high reactivity fuel enhances this mechanism, with increasing intensity as the piston approaches the TDC. The flame propagation mechanism is activated when the heat release from auto-ignition surpasses a specified energy threshold (adjustable through a tunable parameter, $c_{tresh,AI}$), leading to the formation of flame kernels. The number of these kernels corresponds to the total number of injector holes, and their radial positions are assumed to coincide with the zones where auto-ignition occurs first (most likely within the spray region, at the location with the highest concentration of HRF). From these locations, flame fronts propagate spherically and consume the unburned zones, as for example illustrated in Fig. 6. It is noteworthy that the auto-ignition process persists in the unburned zones even after the flame kernels are established and are expanding, leading to the coexistence of both the phenomena. The predominance of one combustion mechanism over the other is determined by their respective rates of progression.

2.3.4. Emission models

The multi-zone model presented in this study is augmented with sub-models specifically designed to predict the most relevant pollutant emissions, including NO, CO, unburned hydrocarbons (uHCs), unburned ammonia (uNH_3), and nitrous oxide (N_2O). These emissions are addressed through three distinct mechanisms:

- Burned zone emission model, that estimates pollutants generated behind the flame front.
- Unburned fuel emission model, that assesses the fraction of fuel that escapes combustion in the chamber.
- Partial oxidation emission model, that calculates products resulting from partial oxidation of the unburned fuel.

The burned zone emission model predicts the concentrations of NO associated with the flame propagation process. This is achieved by first defining the temperature gradient in the burned region, as described in

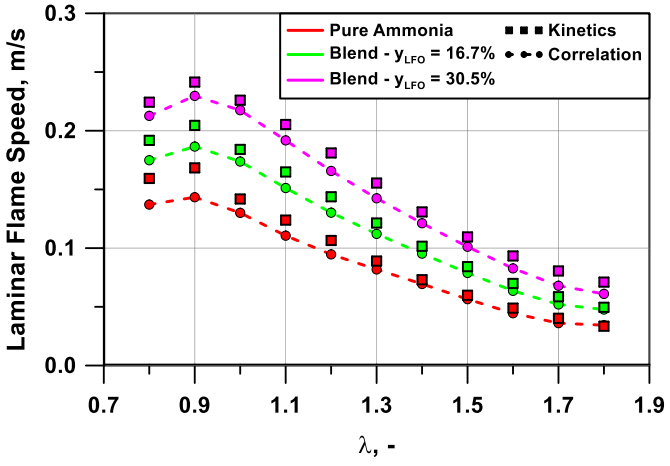

Fig. 5. Comparison between blended S_L and chemical kinetic calculated S_L.

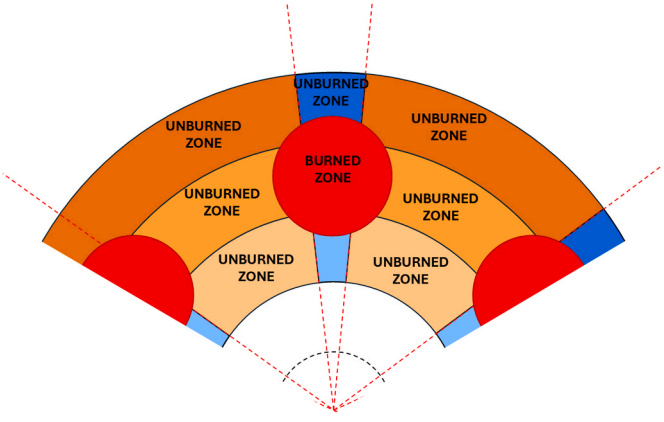

Fig. 6. Flame propagation schematization.

Ref. [97]. At regular time intervals from the initialization of the burned zone, the mass entrained by the flame front during that interval is tracked, along with its pressure, composition, and temperature. Based on these parameters, temperature evolution is computed under adiabatic conditions, also considering composition at equilibrium in the burned gas. For each packet of entrained mass, a simplified kinetic mechanism is applied to determine pollutant concentrations. To maintain energy balance in the burned gas, a thermal boundary layer is also considered. NO formation/destruction is modeled using the simplified kinetic mechanism proposed in Ref. [98], for which a tuning constant, c_{NO}, is utilized to modulate the chemical kinetic rates. It is worthwhile to underline that the adopted approach only describes the so-called thermal NO formation mechanism, which activates above 1600 K and leads to the reaction between molecular nitrogen and oxygen contained in the burned gas. In the case of ammonia combustion, the molecular nitrogen available in the burned gas results from the combination of the nitrogen present in the air and the nitrogen generated from the ammonia combustion itself. For this reason, the thermal NO formation mechanism implemented in the model is capable to calculate a certain part of the NO production from the fuel. On the contrary, other mechanisms of NO formation within the flame front from the fuel itself are not taken into account. These are regulated by a complex chemistry, as described in Refs. [99–101]. A real-time computation of flame chemistry is beyond the scope of this work, also in the perspective of not compromising the computational efficiency typical of phenomenological models, and hence the numerical results shown in the following do not include these possible NO sources.

A detailed model is implemented to estimate unburned fuel emissions, specifically uHCs and uNH_3. This approach accounts for processes such as the filling and emptying of the piston ring-pack crevices, flame quenching near cylinder walls, and fuel post-oxidation [102,103]. The cylinder model framework is extended by incorporating an additional volume to represent the piston crevice region. Using a filling/emptying methodology, the exchanges of mass, species, and energy between the cylinder and crevice volume are computed. The fraction of fuel that escapes combustion due to flame extinction at the cylinder walls is estimated by computing the quenching distance, based on the correlation provided in Ref. [104] and modulated through a tuning constant (c_{quench}) as expressed in Refs. [102,103]. After combustion is complete, any residual unburned fuel in the cylinder is subject to post-oxidation. This process is modeled using a "boundary layer" approach, which assumes that escaped fuel collects in a specific portion of the cylinder, along with a tunable proportion of burned gas (modulated with tuning constants, respectively, $k_{oxid,crev}$, and $k_{oxid,quench}$), as expressed in Refs. [102,103]. Different oxidation tuning constants are adopted for uHCs and uNH_3, respectively. The conditions for post-oxidation, including thermodynamic state and local concentrations of fuel and oxidizer, are determined in this boundary layer. The post-oxidation process is governed by a simplified one-step reaction mechanism, represented mathematically as shown in Eq. (18) for a generic unburned fuel species (*uFuel*).

$$-\frac{d[uFuel]}{dt} = Ae^{\frac{-E_a}{RT}}[uFuel]^{\alpha}[O_2]^{\beta} \tag{18}$$

In this equation, the generic unburned fuel consumption rate, $\frac{d[uFuel]}{dt}$, is expressed in $\frac{mol}{cm^3 s}$, the reactant concentrations, $[uFuel]$ and $[O_2]$, in $\frac{mol}{cm^3}$, while E_a is expressed in $\frac{J}{mol}$. The constants of the one-step reaction are specified according to the fuel under consideration. For uHCs the correlation in Ref. [105] is adopted, while for uNH_3 the correlation is developed on the basis of chemical kinetic calculations performed in a homogeneous reactor with the same kinetic scheme adopted for the TKI offline calculations [86]. The values are reported in Table 6.

Table 6
One-step rate parameters.

Fuel	A	E_a	α	β
LFO	5.1E11	30.0	0.25	1.5
Ammonia	4.53E12	31.1	1.17	0.65

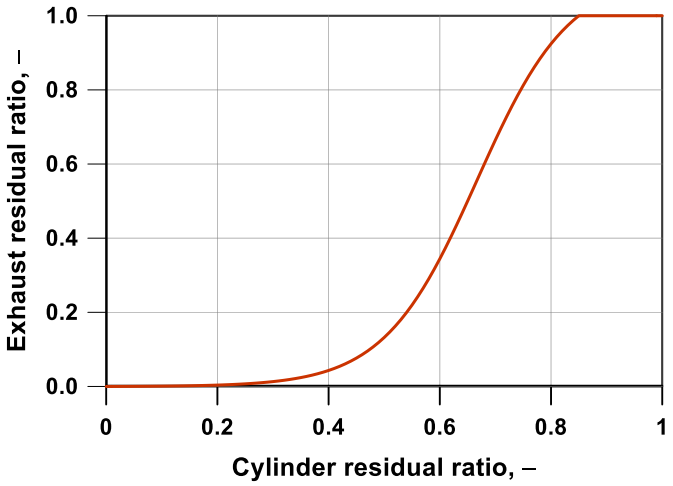

Fig. 7. S-Shape function adopted in the model framework.

The model incorporates the transport of uHC and uNH_3 along the exhaust system, integrating an additional mechanism to define the gas composition at the exhaust valves [102]. This mechanism models the scavenging process in the cylinder using an "S-Shape" function, which determines the exhaust residual ratio based on the in-cylinder burned gas fraction (cylinder residual ratio), as represented in Fig. 7. This modeling framework enhances the accuracy of exhaust gas composition predictions, improving the representation of unburned fuel transport and its impact on emissions.

Some works in the literature underline that one mechanism leading to the formation of both N_2O and CO is the incomplete oxidation of the fuel, ammonia and LFO, respectively, escaped from the regular combustion [23]. On the basis of this observation, in the presented model, a tunable fraction of post-oxidized LFO and ammonia is converted into CO and N_2O, respectively, modulated by the tuning parameters k_{CO} and k_{N2O}.

2.4. Engine model setup and tuning

The engine model in the simulation framework replicates key components, including the intake and exhaust piping systems, the ammonia supply line, the direct injector for light fuel oil, the cylinder, and the intake and exhaust valves. For simulation configuration, boundary conditions are established using measured pressure and temperature levels in the intake and exhaust environments. Additionally, the quantities of LFO and ammonia, along with the timing and duration of LFO direct injection, are specified based on experimental data. The initial stage of model calibration involves determining the optimal number of zones. While increasing the number of zones can enhance accuracy, it also raises computational demands. Preliminary studies conducted on a similar engine [42,43] revealed that a radial segmentation into 80 zones achieves solution invariance, providing an effective balance between precision and computational efficiency. Accordingly, this configuration is adopted in the present study.

The spray and droplet evaporation model does not involve any tuning with respect to their original formulations, presented in the previous sections. The only adaptation concerns the description in the spray model of the jet interaction with the cylinder walls, consisting in assigning the values to parameters $k_{out,spray}$ and s_0 in Eq. (12). As for multi-zone cylinder model and the combustion model, the calibration process involves optimizing the tuning constants associated with

diffusion mechanisms between zones ($k_{diff,m}$, $k_{diff,q}$) and the flame propagation model (c_{trans}, c_{wrk}, c_{xwc}).

Model calibration is performed across five operating conditions, corresponding to the engine load sweep detailed in Table 2. These operating points are selected for model calibration since the load sweep, among the other considered sweeps, is the most challenging engine setting variation to be replicated by the model adopting the same set of tuning constants. This is because of the simultaneous and substantial changes in many of the engine setting parameters, such as pressure at the intake (related to the engine load level), injection timing and duration, LFO content over the total fuel amount, and intake valve closure timing (see Table 2). In all other sweeps these settings are modified in many cases individually and sometimes to a smaller extent.

Defined as an optimization problem, the objective of the optimization is to minimize the integral error between experimental and simulated heat release rates across all operating cases, with the tuning constants employed as optimization variables. The resulting optimized constants, presented in Table 7, are subsequently applied to additional cases to assess and validate the robustness of the developed model. It is worthwhile noting that the identified constants for flame propagation description are in line with those adopted to a similar engine operated in RCCI mode but supplied with natural gas instead of ammonia [42,43]. Those are also similar to the value identified for a premixed engine supplied with gasoline [92]. Although these arguments cannot be considered a real and proper validation, at least demonstrate the versatility of the adopted flame propagation model in various contexts. As for spray model calibration, no 3D CFD or experimental data are available to explicitly validate the correctness of the identified constants. Anyway, the proper working of the identified model calibration in all operating conditions can be assumed as an indirect verification, considering that experimental dataset includes engine settings with various injection timings and engine loads (with different cylinder densities at the injection event).

As for the emission models, the constants of the models are defined through a trial-and-error procedure and fixed for all the tested operating conditions. The optimized values are reported in Table 8. Regarding the scavenging model, the S-Shape function adopted in the simulation is reported in Fig. 7.

3. Results and discussion

In this section, the validation of the presented 0D models and the associated outcomes will be displayed. Firstly, the validation of the spray model compared to the experimental spray chamber experiments will be depicted. Thereafter, some insight into the model outcomes will be shown. To conclude, the validation of the 0D combustion and pollutant model in terms of global and detailed outputs will be performed.

3.1. Spray model validation

The validation of the jet model against the experimental outcomes is illustrated in Fig. 8. The results depicted in this figure represent extreme and medium operating conditions of two specific test cases (T1 and T5) from the experimental test matrix (refer to Table 5). Operating conditions not explicitly presented exhibit behaviors falling between these extremes and are omitted for brevity. Fig. 8 presents a comparison between numerical and experimental results for spray tip penetration. The figure demonstrates that the model successfully replicates experimental spray penetration trends with satisfactory accuracy. In detail, the initial tip penetration is predicted with excellent precision, thanks to the imposition of the trapezoidal profile, that has a strong influence on this phase of the spray evolution. Furthermore, the model effectively captures the acceleration in spray penetration observed with increased injection duration, further demonstrating its predictive capabilities. As already mentioned in section 2.2, it is worthwhile underlining that the optical limit of the adopted spray chamber is about 100 mm. Hence, the flattening of the experimental trends in Fig. 8 is not representative of the spray tip slowdown, but it only depends on a misleading post-process of the images when the spray tip reaches the optical limit.

Table 7
Diffusion, flame propagation and spray tuning constants of the model.

Tuning constant	Value	Tuning constant	Value
$k_{diff,m}$	0.016	$k_{diff,q}$	0.019
$k_{out,spray}$	1.100	s_0	0.781
c_{trans}	0.995	c_{wrk}	3.775
c_{xwc}	0.900	$c_{tresh,AI}$	250 J

Table 8
Emission models tuning constants.

Tuning constant	Value	Tuning constant	Value
c_{NO}	5.00	c_{quench}	2.00
$k_{oxid,crev,uHC}$	0.20	$k_{oxid,crev,uNH3}$	1.20
$k_{oxid,quench,uHC}$	0.15	$k_{oxid,quench,uNH3}$	0.60
k_{N2O}	4.80e-4	k_{CO}	0.36

To provide a comprehensive evaluation, Fig. 9 presents the time-averaged absolute error between numerical predictions and experimental spray penetration profiles across all test cases listed in Table 5. In the majority of cases, the error remains below 5.0 mm, with an overall average of 3.8 mm. These results underscore the robustness of the adopted methodology in capturing the influence of key operating parameters. This robustness is achieved through the implementation of the spray cone angle correlation (refer to Eq. (10)) and the trapezoidal injection profile, which incorporates the correlation of the discharge coefficient and the ramp duration (see Eq. (11)). Greater errors emerge in cases with shorter injection durations, where probably the adopted trapezoidal profile used to describe the injection law is less representative of the real counterpart.

3.2. Detailed analysis

Upon completing the tuning process, the model analytical capabilities become evident through the detailed insights it provides. For instance, the radial fuel stratification in the cylinder can be examined, distinguishing between zones inside and outside the spray region. Fig. 10 illustrates the evolution of the LFO mass distribution, normalized with respect to the total amount of fuel mass, in the cylinder during and after injection for Case #4. In the first frame, captured during the injection, there is a remarkable concentration of LFO in the initial in-spray zones, gradually diminishing along the spray axis. At this stage, the spray jet has not yet reached the cylinder walls, resulting in almost null LFO presence in the out-spray zones. The second frame, corresponding to the EOI, shows a decline in LFO concentration in the initial in-spray zones due to jet inertia. From this point onward, subsequent frames reveal a progressive reduction in LFO concentration in the in-spray zones, with fuel accumulating along the cylinder walls. Additionally, a little fraction of the LFO disperses into out-spray zones adjacent to the wall. This redistribution of fuel near the cylinder wall is facilitated by the out-spray mechanism expressed in Eq. (12). Under these operating conditions, the LFO remains predominantly concentrated in the spray region, consistent with the results of earlier studies [27,39]. Fig. 11 presents a similar analysis for Case #15, with comparable observations but some differences. For instance, during injection, the in-spray zones exhibit a similar penetration but a lower LFO concentration due to the bigger spray cone angle, the higher in-cylinder density, and the lower amount of injected fuel. Furthermore, the sequence of images highlights that the fuel barely touches the walls at EOI, and the out-flow mechanism begins its action later than Case #4, resulting in a less uniform fuel distribution.

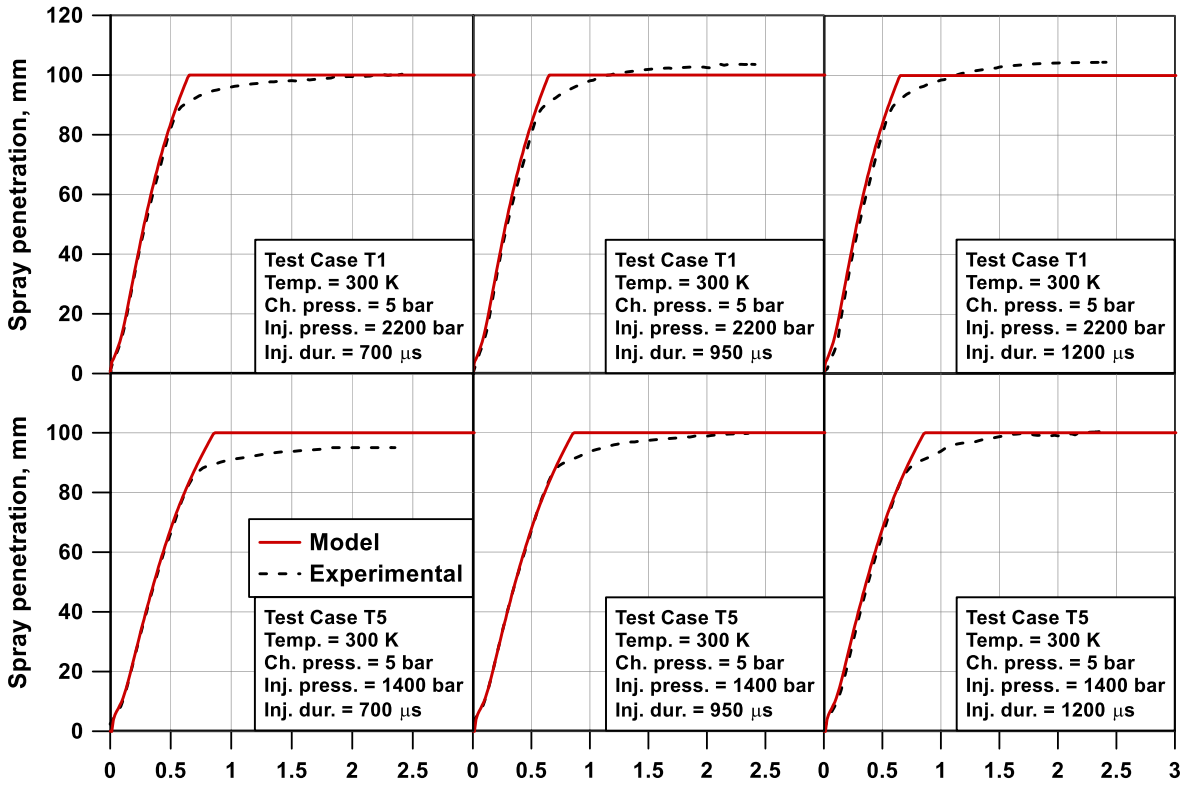

Fig. 8. Numerical/experimental comparison of spray penetration for an injection duration sweep of Test Case T1 (top) and T5 (bottom).

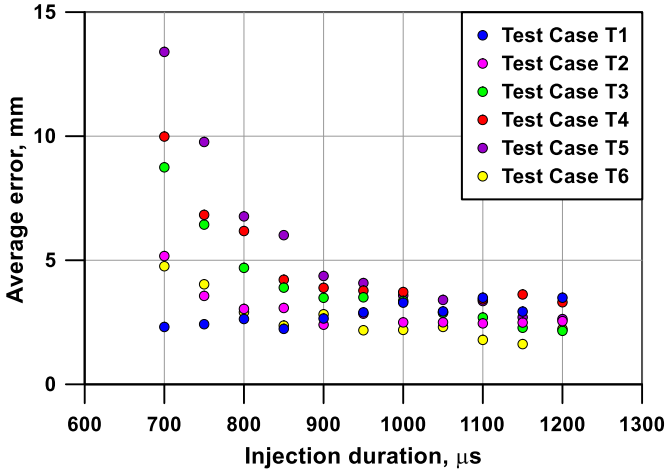

Fig. 9. Absolute average error between experimental and numerical spray tip penetration for spray chamber test cases.

It is worthwhile noting that fuel distributions 40 CADs after the end of the injection in Figs. 10 and 11 are almost consolidated and will not evolve anymore in the subsequent time, and the auto-ignition of the most reactive zone will occur later during the engine cycle. In the light of this consideration, transient effects in spray modeling may have in the presented cases a marginal influence on the combustion prediction, while it is more relevant to reproduce as realistically as possible the allocation of the LFO when the combustion starts.

The combustion model formulation accounts for the simultaneous occurrence of both flame propagation and auto-ignition, determining the dominant fuel consumption mechanism based on local thermodynamic conditions, equivalence ratio, and fuel distribution. The interaction between these two combustion processes is illustrated in Fig. 12, which presents the normalized heat release contributions for two operating conditions from Table 2: test Cases #4 (left) and #15 (right). In both cases, flame propagation is the predominant combustion mode, while auto-ignition primarily acts as a trigger. In both cases, the flame initiates from the zones within the spray closer to the cylinder liner where the LFO accumulates. However, a distinction emerges between low-load and high-load conditions. Under low-load operation, auto-ignition contributes to the combustion process, as flame propagation alone is insufficient to fully oxidize the fuel in the final stages. Moreover, the autoignition of unburned charge ahead of the flame contributes to sustaining the flame propagation, which otherwise would have been too slow to complete the combustion process. Conversely, at high load, flame propagation progresses rapidly enough to dominate fuel consumption throughout the combustion process, even in its later stages, effectively inhibiting the possible onset of auto-ignition of the unburned charge.

3.3. Model validation

The initial step in validating the model involves comparing the predicted overall engine performance parameters with their experimental counterparts. The relative and absolute discrepancies between the numerical predictions and experimental results provide a quantitative measure of the model accuracy. To ensure confidentiality, all presented results are normalized with respect to experimental data obtained at the maximum nominal load operating point (Case #21 in Table 2). Similarly, angular data plots display only the grid discretization explicitly, adhering to confidentiality requirements. In the subsequent figures, groups of operating conditions are represented by color-coded circles, corresponding to the parameter sweeps outlined in Table 2. Specifically, blue circles represent the relative intake valve closure sweep at low load conditions ($\Delta\theta_{IVC}$ LL) (Cases #1 to #3), magenta circles denote the relative λ sweep at low load conditions ($\Delta\lambda$ LL) (Cases #4 to #9), green circles signify to the normalized injection duration sweep at low load conditions (τ_{Inj} LL) (Cases #10 to #12), red circles correspond to the relative λ sweep at high load conditions ($\Delta\lambda$

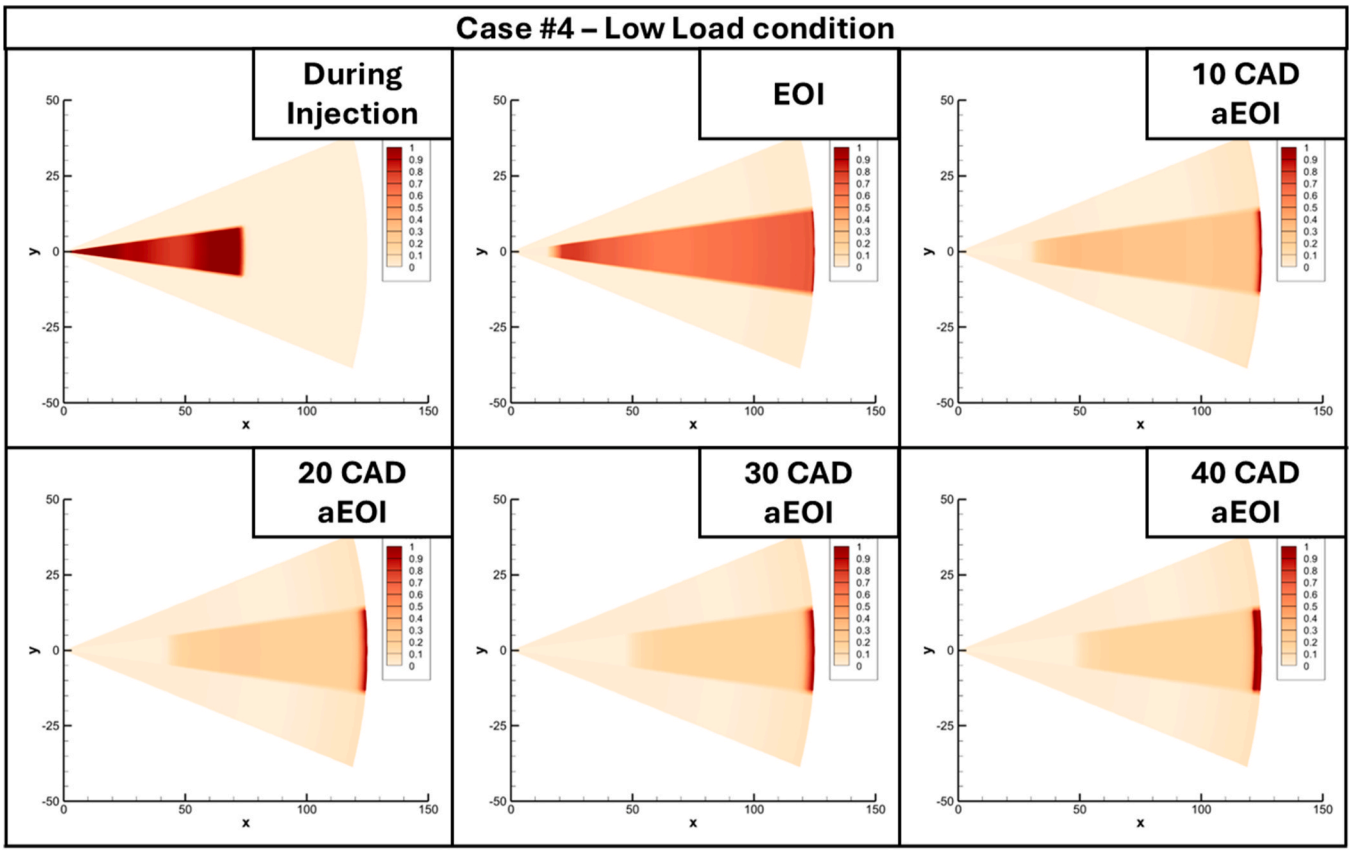

Fig. 10. Graphical representation of the LFO mass fraction evolution inside the combustion chamber during and after the injection phase for Case #4.

HL) (Cases #13 to #14), purple circles indicate the relative injection timing sweep at high load conditions ($\Delta\theta_{Inj}$ HL)(Cases #15 to #16), and the black circles represent the load sweep (Cases #17 to #21). Note that the size of the symbol increases with the level of the varied parameter within each sweep (in case of negative value, the size increases moving towards zero-level).

The comparison between numerical and experimental air mass flow rates is depicted in Fig. 13 (right), demonstrating a satisfactory level of model accuracy, with all data points falling in a 5 % error margin. The relative error of 0.87 % indicates that the intake and exhaust pipe geometries are accurately represented, and the valve flow coefficients are appropriately specified. Similarly, Fig. 13 (left) shows that the IMEP is well predicted, remaining in the acceptable 5 % error margin. This results in a relative error of 2.38 %. The accurate predictions of both IMEP and air mass flow rates suggest that the model provides a reasonable estimation of wall heat losses.

The predictive capability of the combustion model is illustrated in Fig. 14, comparing the model results to experimental data for the early combustion phase (CA_5, left) and the combustion duration ($CA_{5\text{-}75}$, right), defined as the angular difference between CA_{75} and CA_5. Regarding the initial combustion stage, the model shows a good level of accuracy, with an absolute error of 2.25 CAD, and almost all the cases remain in the 5 CAD error band. However, the model presents a general anticipation of the early combustion stage. This discrepancy is largely imputable to an overestimation of the initial heat release due to auto-ignition, resulting in an anticipation of the beginning of the flame front propagation. For the combustion duration, the model demonstrates reasonable accuracy, with an absolute error of 2.78 CAD and almost all the cases falling in the 5 CAD error band. A general tendency to overprediction of the combustion duration is visible in most cases. This error can be attributed to the assumption of spherical flame propagations. In reality, it is plausible to argue that flame fronts evolve into more complex shapes, influenced by the spray volumes. However, the model effectively captures combustion duration and centering across a wide range of operating conditions, including variations in equivalence ratios, LFO fractions, and in-cylinder thermodynamic states (pressure and temperature at IVC). This highlights its robustness and utility in predicting combustion behavior under diverse scenarios.

The accuracy of the predicted combustion evolution is further corroborated by comparing the crank angles at maximum pressure and the corresponding peak pressure levels, as depicted in Fig. 15 (right and left, respectively). The majority of the predicted data points fall in a 5 CAD error margin for crank angles and a 10 % error margin for peak pressure levels. This consistency highlights the reliability of the model estimations, achieved without the need for case-specific parameter adjustments.

To enforce the physical background of the developed model, the numerical/experimental validation of exhaust pollutant emissions is discussed in the following figures.

Fig. 16 depicts the comparison between numerical and experimental outcomes for uHC (a), uNH_3 (b) and N_2O (c), exhaust concentrations. The numerical uHC concentration prediction results quite accurate compared to the experimental outcomes, with an average relative error of 23.94 % and with the model capable to replicate the experimental trends with satisfactory accuracy. Interestingly, the model is able to detect the growth in uHC emissions as the load decreases or λ increases. The prediction of uNH_3 is quite accurate, resulting in an average relative error of 20.85 %, and demonstrating the predictive capabilities of the developed model in both trends and values. Maximum levels emerge in the cases within the load sweep in the high load conditions, caused by short-circuiting during valve overlap. On the opposite, the results highlight that the minimum emissions occur as λ increases.

N_2O model estimation is acceptable, leading to a relative error of 25.10 %. The predicted trends are show similarities with the

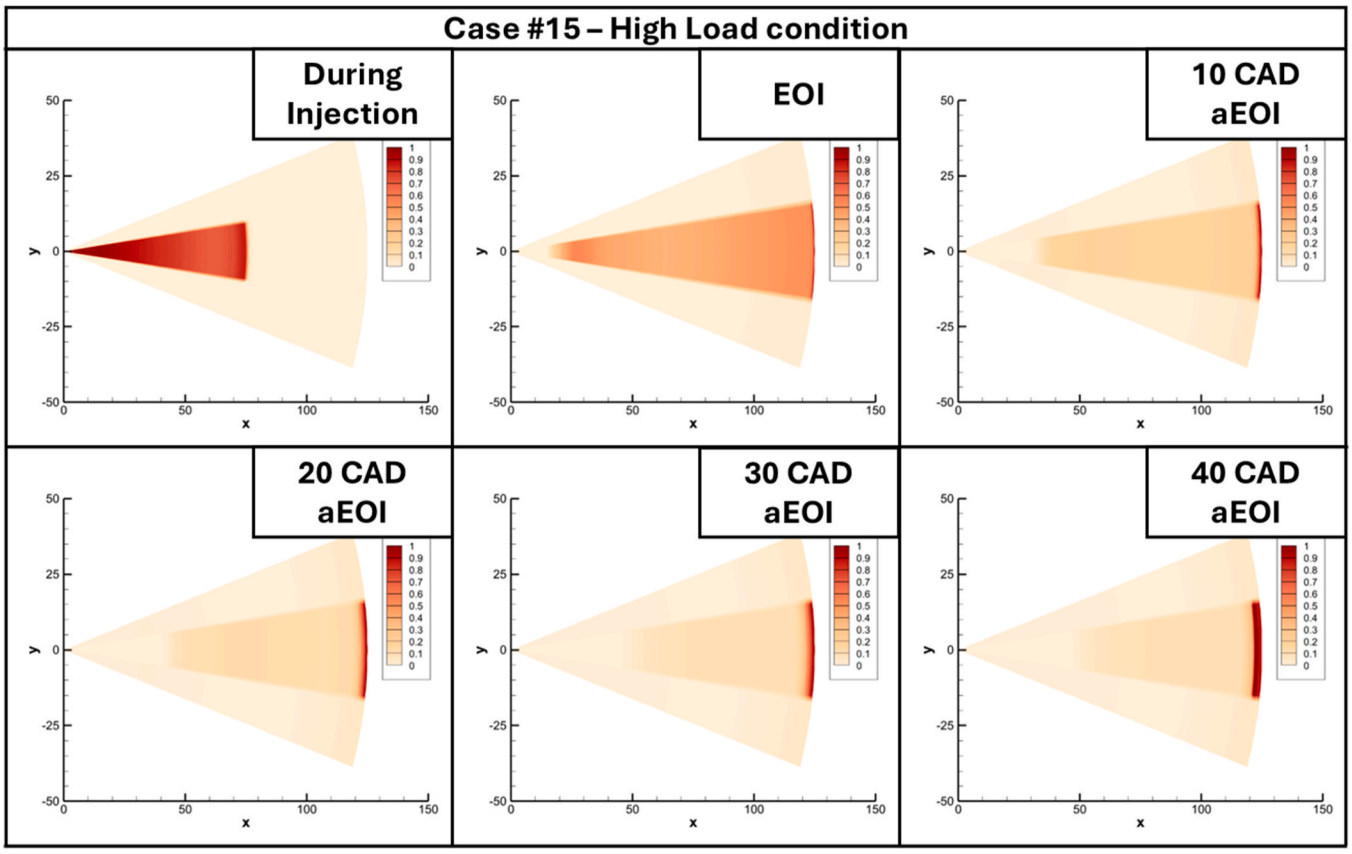

Fig. 11. Graphical representation of the LFO mass fraction evolution inside the combustion chamber during and after the injection phase for Case #15.

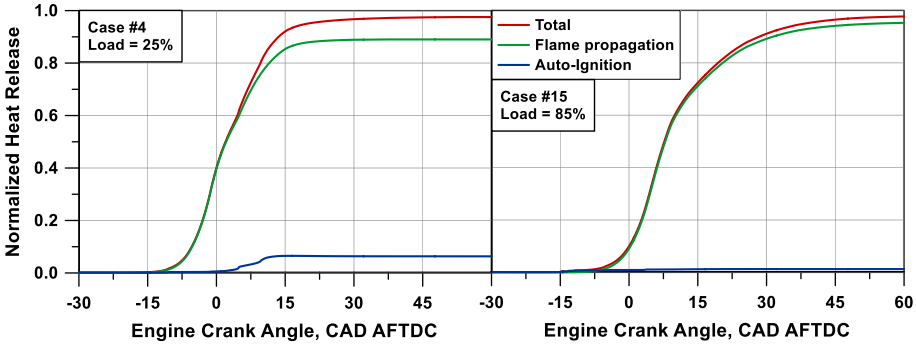

Fig. 12. Normalized heat release repartition between flame propagation and auto-ignition at low load, Case #4, (left) and high load, Case #15 (right).

experiments, demonstrating the potential of the approach. Anyway, further refinements appear mandatory to better detect the prediction of this pollutant, which is governed by a complex chemistry, as highlighted in Refs. [99–101].

Fig. 17 provides an insight into the outcomes of the unburned fuel model in terms of source contributions for six representative operating conditions. The figure reports under the form of bar charts the splitting between unburned fuel contributions from crevice filling/emptying, flame wall quenching and scavenging mechanisms, also highlighting individual unburned fuel concentrations before and after the post-oxidation process. The levels of molar concentrations are normalized for each case with the total production after the post-oxidation process. As a consequence, total emissions after the post-oxidation process is in all cases equal to 100 %, while the levels before this process are greater. Focusing on the final concentrations, after post-oxidation, the figure highlights that the crevice contribution is the most relevant one for both uHC and uNH_3, especially in low load conditions. The quenching contribution has an impact on the total unburned fuel concentrations mainly in high load conditions, where the flame propagation is the main combustion mechanism. The scavenging effect is visible exclusively in the load sweep conditions and for uNH_3, since these operating conditions exhibits a large valve overlap. For uHC this contribution is null since LFO is injected during the compression phase. As for uHC levels before post-oxidation process, Fig. 17 puts into evidence that the contribution from flame wall quenching is mainly post-oxidized in all cases. The only operating conditions with a relevant uHC from flame wall quenching are the high load cases, where the post-oxidation is less effective being the combustion phased later during the engine cycle (see Fig. 14 (left)). Fig. 17 also highlights that the uNH_3 contribution from crevices is not subjected to relevant post-oxidation, while the uNH_3 from flame wall quenching (before being oxidized) is quite relevant in most operating conditions, but this is highly abated, especially in low load

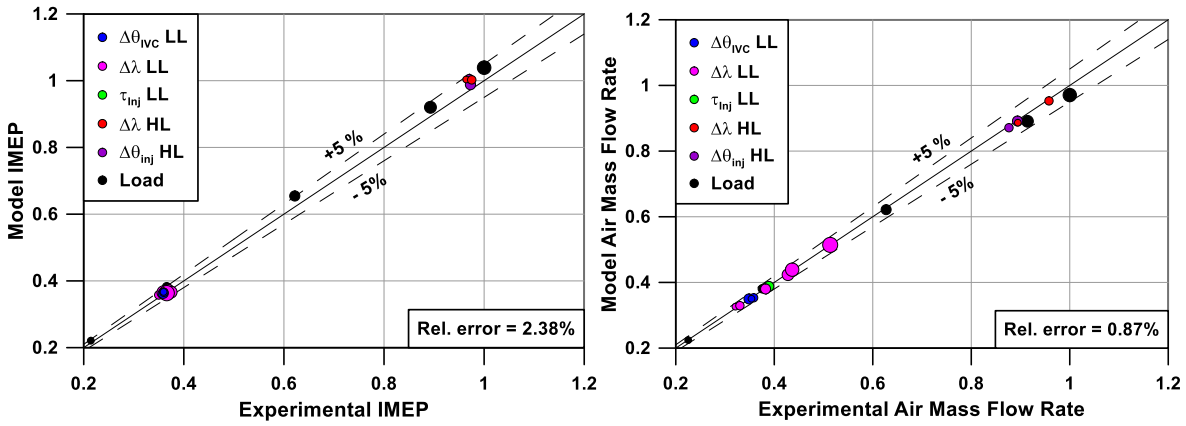

Fig. 13. Comparisons of numerical and experimental outcomes of normalized IMEP (left) and normalized air flow rate (right).

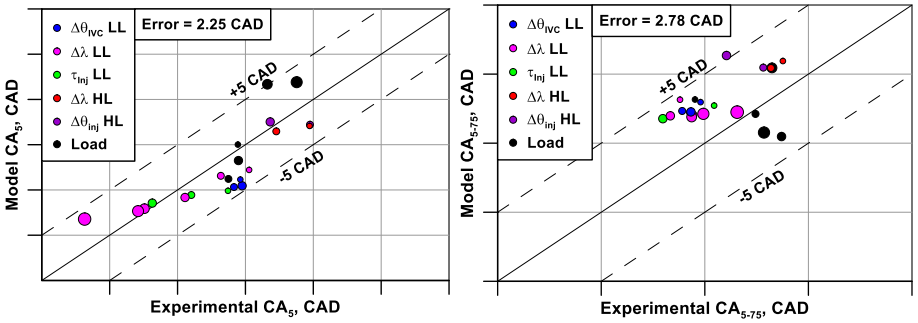

Fig. 14. Comparisons of numerical and experimental outcomes of CA_5 (left) and $CA_{5\text{-}75}$ (right).

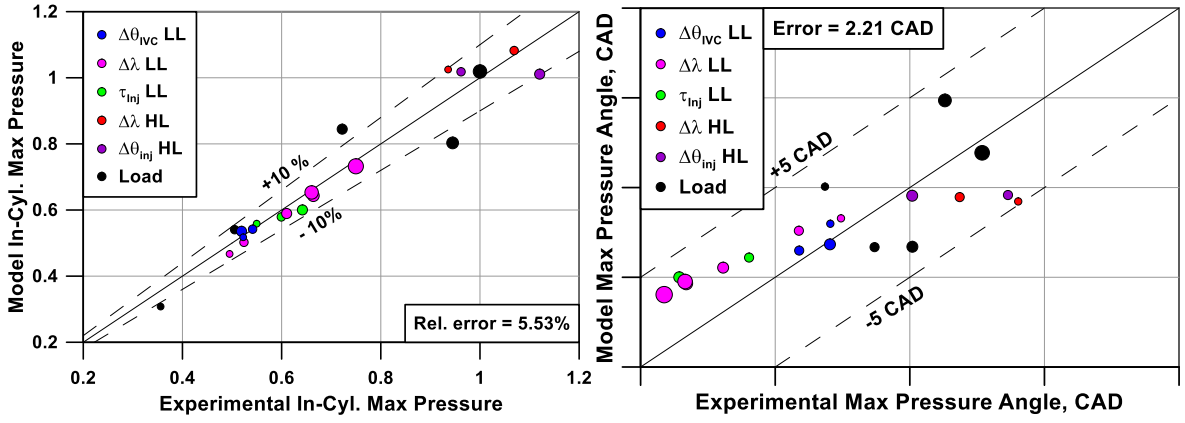

Fig. 15. Comparisons of numerical and experimental outcomes of in-cylinder pressure peak (left) and angle of pressure peak (right).

cases. This is again justified by a more advanced combustion phasing, which determines more favorable conditions for ammonia oxidation. The greatest amount of post-oxidized ammonia occurs in the high load conditions, which are also the operations where the largest amount of N_2O is produced (see Fig. 16 (c)). Again, the capturing of the global trend in N_2O prediction can be considered as an indirect verification of the formation and post-oxidation mechanisms for uNH_3.

Fig. 18 displays the exhaust emissions of NO (left) and CO (right). The NO concentration prediction is below the experimental counterpart in most of the cases, resulting in a relative error of 38.71 %. Experiments evidence that higher NO emissions appear at low load operations, and the model is able to detect this occurrence in a satisfactory manner. The high production of NO is caused in the model prevision by the heat released ahead of the flame, which reflects in increased levels of temperature of the burned gas. This occurrence is less pronounced in the high load conditions, with smaller NO emissions compared to the measured counterparts. The overall NO results can be recognized as acceptable also considering that the mechanism of NO production from fuel is not taken into account. On the opposite, the CO prediction is satisfactory, resulting in a relative error of 20.19 %. The model is still able to perceive the experimental trends in all the operating conditions, with lower CO emissions as the load decreases or λ increases, consistently with similar trends in uHC emissions. It is worthwhile mentioning that the post-oxidation of uHC is in the presented model the main responsible for the CO formation in the lean conditions under study. The satisfactory correlation of CO predictions with the experimental data, as shown in Fig. 18 (right), can be advised as an indirect confirmation of the correctness of the adopted CO formation mechanism and of the

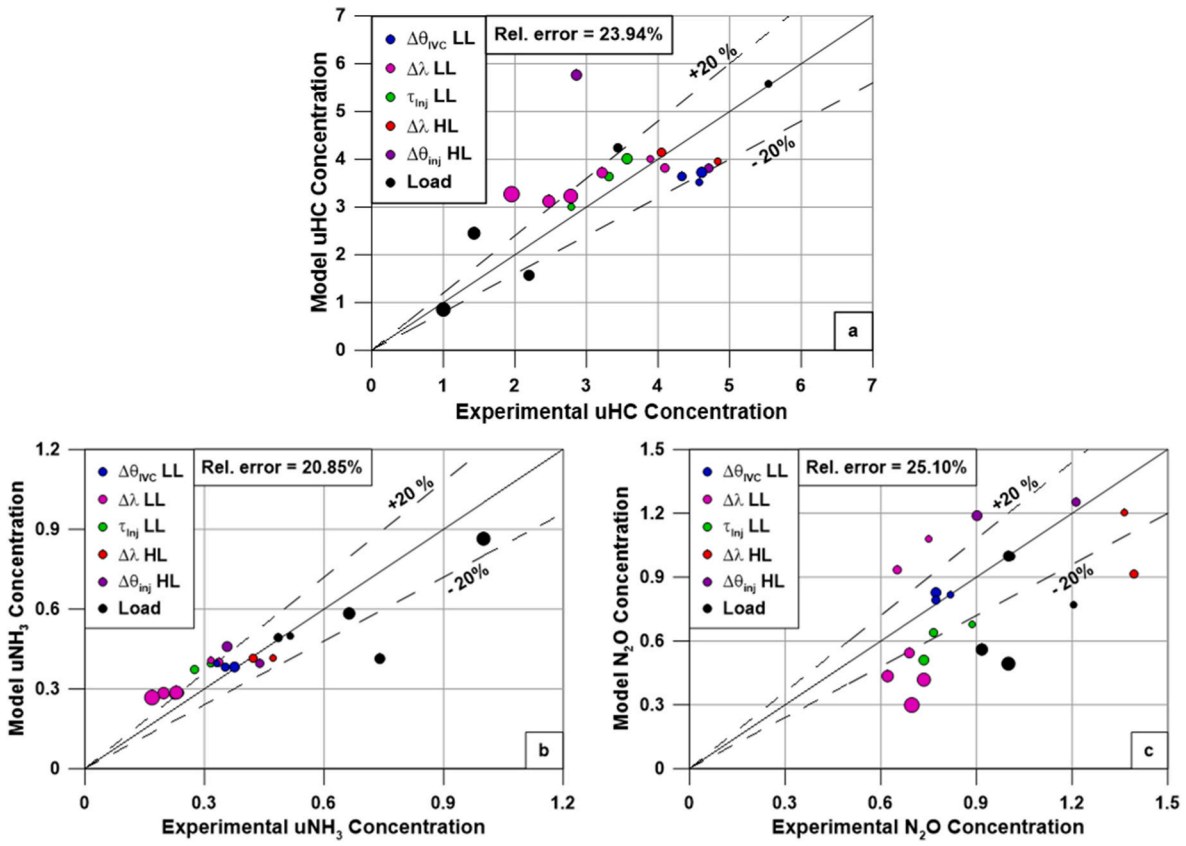

Fig. 16. Comparisons of numerical and experimental outcomes of exhaust concentration of uHC (a), uNH_3 (b) and N_2O (c).

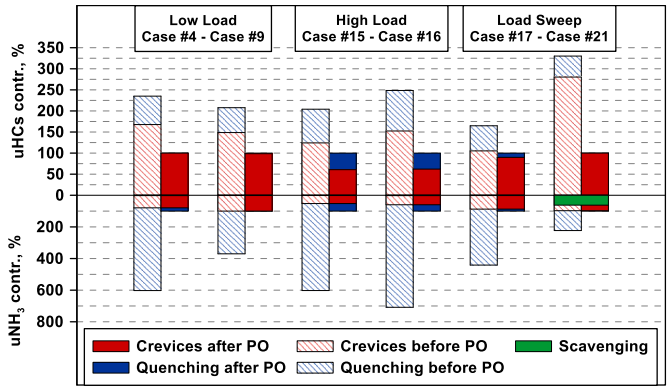

Fig. 17. uHC and uNH_3 model source contributions for Low Load (Case #4, Case #9) High Load (Case #15, Case #16), and Load Sweep (Case #17, Case #21) conditions (all the contributions are normalized with respect to the total exhaust concentration).

production and post-oxidations models for the unburned hydrocarbons.

The combustion model accuracy is further validated through a comparison of numerical and experimental in-cylinder pressure and heat release rates. For clarity, only the extreme cases from the sweeps outlined in Table 2 are presented, while intermediate cases, which showcase engine behaviour between these extremes, are excluded for conciseness. In the figures, experimental data are represented by black dashed lines, while the numerical results are depicted with continuous red lines.

Fig. 19 illustrates the comparison of in-cylinder pressure and normalized heat release rates for the extreme cases of the $\Delta\theta_{IVC}$ sweep at low load conditions (Cases #1 and #3). The comparison demonstrates the satisfactory prediction capabilities of the model. The pressure trace is adequately predicted, together with its peak and phasing. Looking at the heat release rates, the model results exhibit a certain anticipation of the peak phasing and an underestimation of the value compared to the experiments. In addition, a slight knee is visible in the second phase, due to a heat release from auto-ignition, corresponding to what is shown in Fig. 12. To be more precise, towards the combustion completion (see for instance Case #4 in Fig. 12), a relevant amount of heat release comes from the auto-ignition of some zones outside of the spray, rich in LFO (mostly located in the proximity of the cylinder liner, filled by the outflow mechanism describing the spray/wall interaction). The predicted intensity of this second local heat release peak is too intense compared to the experiments, where likely this phenomenon is less pronounced thanks to a more homogeneous distribution and a better mixing with the air of the LFO outside of the spray. Both numerical and experimental results highlight a slight sensitivity to $\Delta\theta_{IVC}$ variation.

Fig. 20 depicts the numerical and experimental in-cylinder pressures and heat release rates for the extreme conditions of the $\Delta\lambda$ sweep at low load (Cases #4 and #9). The numerical pressure trace almost matches the experimental counterpart for the least diluted case, while it is slightly underestimated in the other one, resulting in an adequate sensitivity of the model to the mixture leanness. Again, auto-ignition in the ending part of the combustion appears to be overestimated to some extent.

Fig. 21 shows the numerical/experimental comparison for the extreme conditions of the duration of injection at low load conditions (Cases #10 and #12). Looking at the measured in-cylinder pressure cycles, a DI increase determines earlier and faster combustion. Despite of a lower sensitivity, the model is capable to sense this behaviour.

Moving to the high load sweeps, Fig. 22 represents the comparison between numerical and experimental outcomes for different λ levels (Cases #13 and #14). The model overestimates the pressure evolution and the peak for the first case, while the prediction is accurate in the

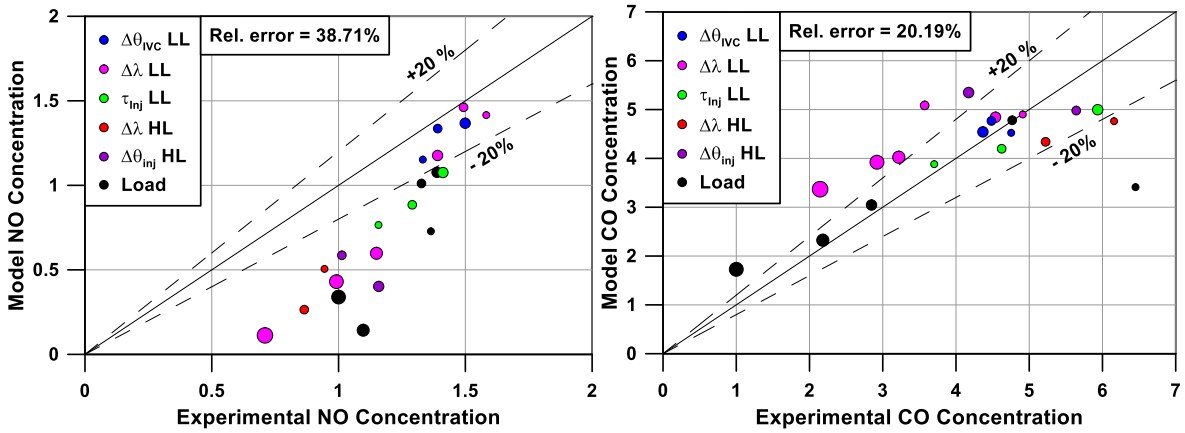

Fig. 18. Comparisons of numerical and experimental outcomes of exhaust concentration of NO (left) and CO (right).

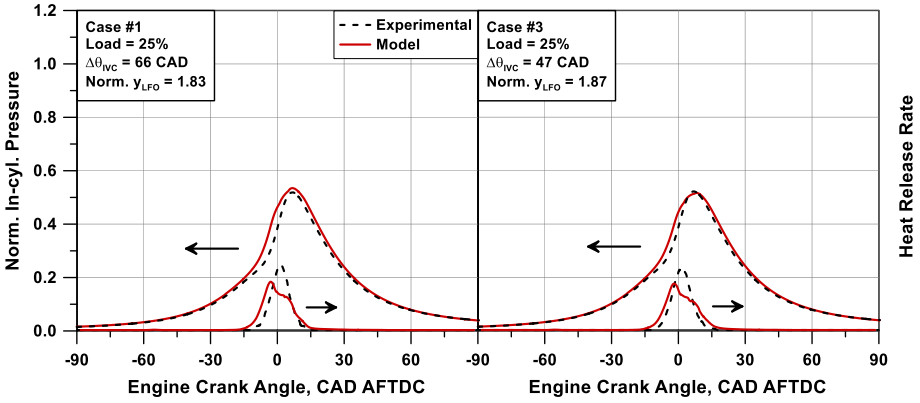

Fig. 19. Comparisons of numerical and experimental outcomes of in-cylinder pressure and heat release rates for Cases #1 (left) and #3 (right).

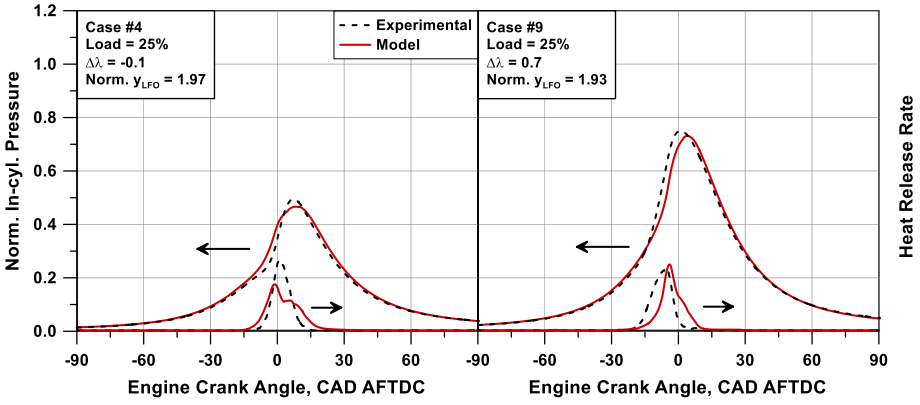

Fig. 20. Comparisons of numerical and experimental outcomes of in-cylinder pressure and heat release rates for Cases #4 (left) and #9 (right).

second one. This trend can be also observed in the anticipation of the heat release peak. It is also possible to notice that the model heat release rates do not show the knee seen in the low load conditions, as illustrated in Fig. 12, but the combustion tail is generally longer compared to the experiments. This aspect can be attributed to an oversimplified description of the combustion chamber geometry, and the consequent interaction between the flame front and the in-cylinder walls. Indeed, the assumption of spherical flames results in the smallest possible area in comparison with any other geometrical configuration.

Fig. 23 illustrates the experimental/numerical comparison for the extreme cases of the $\Delta\theta_{Inj}$ sweep at high-load conditions (Cases #15 and #16). For the first case, the model slightly underestimates the heat release rate peak, resulting in a restrained underprediction of the pressure trace. On the other hand, in the second case the heat release rate is slightly anticipated, but the peak is lower compared to the experiments, resulting in an overestimation of the pressure evolution. The experiments evidence a remarkable sensitivity to the variation of the timing of injection, of six CADs in the presented, which the model only marginally appreciates.

To conclude, the extreme cases of the load sweep (Cases #17 and #21) are compared in Fig. 24. In these conditions, the model slightly underestimates the heat release rate peak and the in-cylinder pressure for the lowest load, but the prediction at the highest load is good, in both the pressure and the heat release rate.

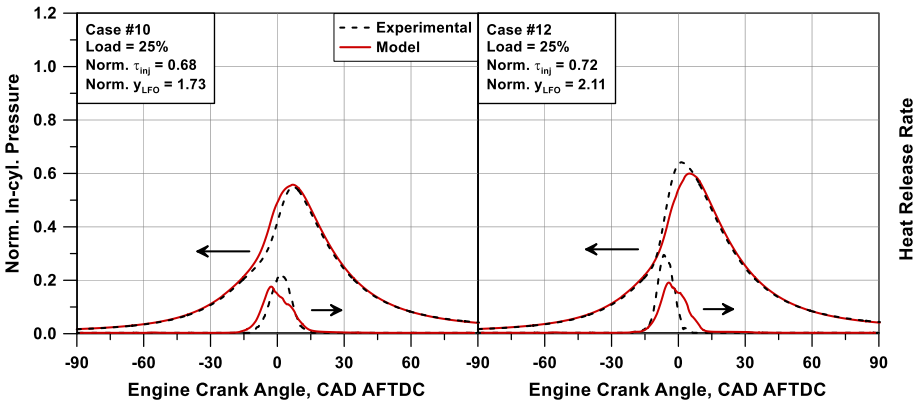

Fig. 21. Comparisons of numerical and experimental outcomes of in-cylinder pressure and heat release rates for Cases #10 (left) and #12 (right).

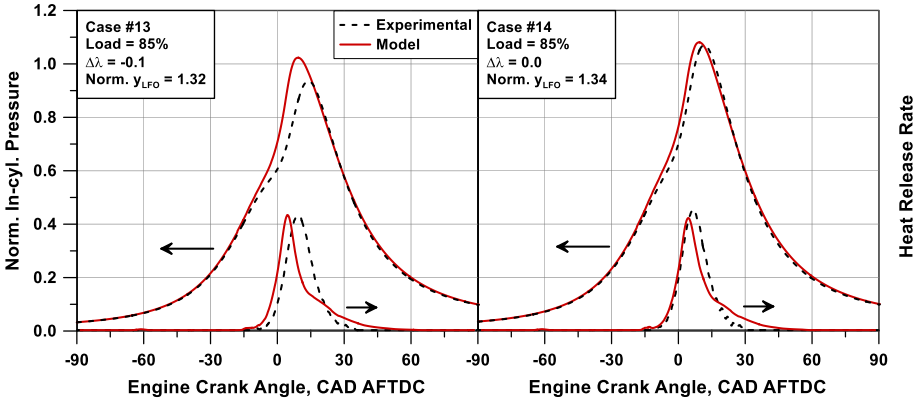

Fig. 22. Comparisons of numerical and experimental outcomes of in-cylinder pressure and heat release rates for Cases #13 (left) and #14 (right).

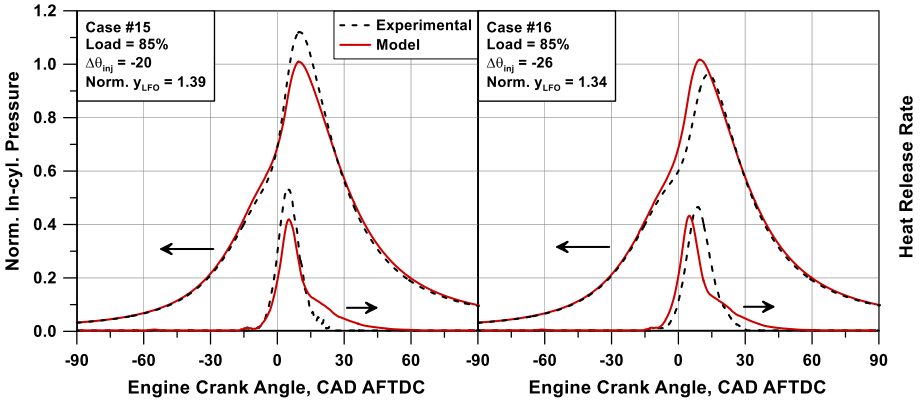

Fig. 23. Comparisons of numerical and experimental outcomes of in-cylinder pressure and heat release rates for Cases #15 (left) and #16 (right).

As a final remark, it is not worthwhile to underline that, despite some limitations in appreciating the influence of some operating parameters, the model physical background can be deemed as adequately robust, considering the variety of the investigated operating conditions and the absence of a case-by-case tuning of the model constants.

4. Conclusions and outlook

This study presents a refined combustion model specifically designed for engines operating in RCCI mode with ammonia/LFO blends, accounting for both fuel auto-ignition and flame propagation processes. The model employs a complex zonal structure that combines cylindrical axisymmetric zones with conically shaped zones, enabling precise estimation of in-cylinder temperature and fuel stratification. In each zone, species and energy balance equations are solved to determine the thermochemical evolution of the combustion chamber. The framework integrates various sub-models, categorized into three primary groups.

The first group comprises zonal interaction and evolution models, including the zonal diffusion model, spray model, droplet evaporation model, and heat transfer model. This category enables the 0D model to capture inhomogeneities in the combustion chamber. The second group encompasses combustion models, which consist of the ignition and flame propagation models responsible for calculating the progression of the combustion process. The ignition model utilizes a tabulated chemistry approach to enhance computational efficiency, while flame propagation is represented by a fractal combustion framework. Finally, the

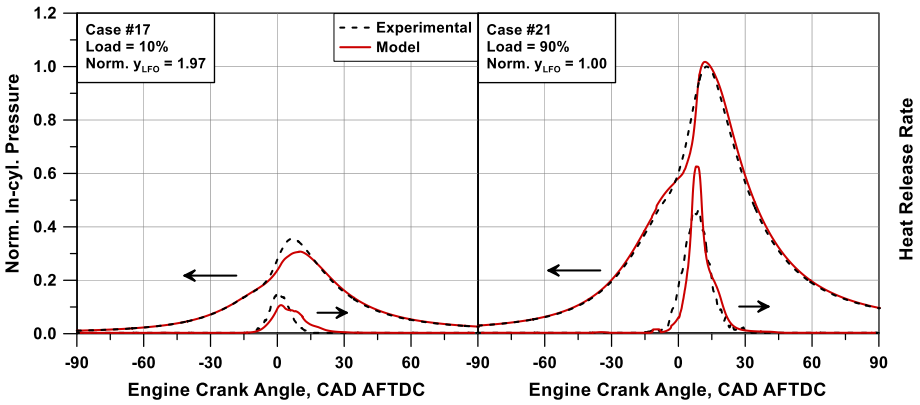

Fig. 24. Comparisons of numerical and experimental outcomes of in-cylinder pressure and heat release rates for Cases #17 (left) and #21 (right).

third group includes an emissions model, integrating a burned zone kinetic model, an unburned fuel emission model, and a partial oxidation model to predict pollutants such as CO, NO, N_2O, uHC and uNH_3.

The 0D model is tuned using data from a single-cylinder research engine designed for marine applications, fueled with ammonia via intake port injection and LFO through a direct high-pressure injector, and data from constant-volume spray chamber. The predictive capability of the combustion model is validated by comparing global performance parameters and combustion characteristic angles with experimental data. The main results reached by the 0D model are summarized as follows:

- The spray model is able to replicate experimental spray tip penetration in different ambient and injection conditions. This result is achieved with a cone angle correlation, developed on the basis of experimental information, and a trapezoidal injection rate profile.
- The 0D/1D model achieves errors in 10 % band for global parameters (air flow rate, IMEP, peak pressure) and 5 CAD band for combustion angles in most cases, resulting in satisfactory replication of the intake and exhaust systems, heat transfer and combustion phasing.
- The emissions model achieves errors mostly in 20 % band for all the pollutants, resulting in a satisfactory sensitivity to all the operating conditions.
- For further validation, the model's consistency is supported by its ability to replicate instantaneous trends such as pressure cycles and heat release rates, particularly in predicting the balance between ignition and flame propagation. Some inaccuracies are noted in heat release rate levels, with a tendency for early combustion centering in specific scenarios. Numerical results reveal that flame propagation predominantly governs heat release in all the cases, while auto-ignition exhibits a visible contribution to heat release exclusively at low loads, although it is fundamental to initiate the flame propagation.

This approach demonstrates its reliability as a tool for predicting engine performance and emissions under RCCI operation with ammonia, adapting effectively to key engine parameters. Future development will focus on the following aspects:

- Incorporation of a diffusion flame combustion model to improve early-stage heat release predictions and extend capabilities to Diesel-like operations with direct injection near TDC. Achieving this requires addressing combustion interactions with droplet evaporation, considering limitations imposed by fuel evaporation rates.
- Interactions between spray jets and in-cylinder flow fields, including squish and swirl motions, which influence fuel distribution and ignition dynamics.
- Integration of multiple injections into the spray jet model, necessitating modifications to mathematical formulations to capture interactions between multiple injection events.
- Improvement of the flame geometry evolution in relation to the conical spray structure. It may mitigate the observed tendency for combustion centering anticipation in certain operating conditions.
- Integration of the flame chemistry description, via tabulation or reduced order reaction schemes, to improve the prediction of NO, directly deriving from ammonia combustion, and of N_2O.

Greeks	
Δ	Difference
ΔH_{vap}	Heat of vaporization
Γ_{MAX}	Length scale of maximum flame wrinkling
Γ_{MIN}	Length scale of minimum flame wrinkling
θ	Angle
λ	Air/fuel equivalence ratio
λ_t	Total conductivity
Ξ	Wrinkling factor
ρ	Gas density
τ	Time duration
Φ	Fuel/air equivalence ratio
Acronyms	
0D-1D-3D	Zero-One-Three-dimensional
ACC	Active Combustion Control
AFTDC	After Firing Top Dead Center
B_M	Mass Spalding number
B_T	Thermal Spalding number
CAD	Crank Angle Degree
CA_{5-75}	Combustion Duration
CA_{50}	50 % of Mass Fuel Burned Crank Angle
CFD	Computational Fluid Dynamic
CO	Carbon monoxide
CoV	Coefficient of Variation
CO_2	Carbon dioxide
EOI	End of Injection
EU	European Union
GHG	Greenhouse Gas
GWP	Global Warming Potential
HL	High Load
HFO	Heavy Fuel Oil
HRF	High Reactivity Fuel
HRR	Heat Release Rate
IEEE	Institute of Electrical and Electronics Engineers
IMEP	Indicated Mean Effective Pressure
IMO	International Maritime Organization
IVC	Intake Valve Closure
LED	Light-Emitting Diode
LFO	Light Fuel Oil
LHV	Lower Heating Value
LL	Low Load
LRF	Low Reactivity Fuel
LTC	Low Temperature Combustion
MW	Molar Weight

(*continued on next page*)

(*continued*)

NG	Natural Gas
NH_3	Ammonia
NO_x	Nitrogen Oxides
NO	Nitric Oxide
N_2O	Nitrous Oxide
N_{SPC}	Number of Species
N_z	Number of Zones
RCCI	Reactivity Controlled Compression Ignition
RON	Road Octane Number
SCE	Single Cylinder Engine
SCR	Selective Catalytic Reduction
SOI	Start of Injection
TDC	Top Dead Center
TKI	Tabulated Kinetic of Ignition
uFuel	Generic unburned fuel species
uHC(s)	Unburned Hydrocarbon(s)
uNH_3	Unburned Ammonia
Symbols	
A	Area
c	Liquid specific heat
c_D	Discharge coefficient
c_{NO}	Flame-derived NO tuning constant
c_p	Specific heat at constant pressure
c_{quench}	Quenching distance tuning constant
c_{trans}	Laminar-to-Turbulent transition multiplier
$c_{tresh,AI}$	Heat release from auto-ignition treshold
c_{wrk}	Wrinkling factor multiplier
c_{xwc}	Wall combustion transition multiplier
D	Mass diffusivity
d	Diameter
D_3	Fractal dimension
E	Internal energy
H_t	Convective heat transfer coefficient
h	Specific enthalpy
k	Thermal conductivity
k_{CO}	Partial oxidation-derived CO tuning constant
$k_{diff,m}$	Mass diffusive transfer multiplier
$k_{diff,q}$	Heat diffusive transfer multiplier
k_{N2O}	Partial oxidation-derived N_2O tuning constant
$k_{out,spray}$	Spray out-flow multiplier
$k_{oxid,crev,uHC}$	Crevice post-oxidation tuning constant for uHC
$k_{oxid,crev,uNH3}$	Crevice post-oxidation tuning constant for uNH_3
$k_{oxid,quench,uHC}$	Quenching post-oxidation tuning constant for uHC
$k_{oxid,quench,uNH3}$	Quenching post-oxidation tuning constant for uNH_3
m	Mass
n	Mole
Nu^*	Corrected Nusselt number
p	Pressure
p_{N2O}	N2O molar concentration
p_{N2O2}	Nitrogen-to-oxygen molar ratio in air
Q	Heat transfer/subtracted
R	Molar gas constant
r	Radius
Sh^*	Corrected Sherwood number
S_L	Laminar flame speed
s	Spray axis normalized position
s_0	Initial spray axis normalized position for out-flow
T	Temperature
t	Time
V	Volume
x	Mass fraction
y	Energy fraction
Subscript	
a	Related to ambient

(*continued on next column*)

(*continued*)

AI	Related to auto-ignition
b	Related to burned gas
$chem$	Related to chemistry
$cone$	Related to spray cone
CO_2	Related to CO_2
cyl	Related to cylinder conditions
die	Related to diesel fuel
$drop$	Related to droplet
$evap$	Related to evaporation
$fuel$	Related to fuel
g	Related to gas
i	Related to species
Inj	Related to the injection
IVC	Related to Intake Valve Closure
L	Laminar
LFO	Related to light fuel oil
NH_3	Related to ammonia
N_2O	Related to N_2O
OUT	Related to the zones outside of the spray
$peak$	Related to peak conditions
$prod$	Related to combustion products
r	Related to residual gas
$ramp$	Related to injection ramp
ref	Related to reference conditions
sat	Related to saturation conditions
T	Turbulent
tot	Related to total conditions
u	Related to unburned gas
$umbrella$	Related to umbrella angle
W	Related to wall
z	Related to zones
Superscript	
$diff$	Related to diffusion
$spray$	Related to spray
Accents	
$\dot{}$	Time derivative
$\bar{}$	Average value

CRediT authorship contribution statement

Vincenzo De Bellis: Writing – review & editing, Writing – original draft, Validation, Supervision, Software, Methodology, Conceptualization. **Massimiliano De Felice:** Writing – review & editing, Writing – original draft, Validation, Software, Methodology, Conceptualization. **Enrica Malfi:** Writing – review & editing, Validation, Supervision, Software, Methodology, Conceptualization. **Fabio Bozza:** Writing – review & editing, Supervision, Methodology, Conceptualization. **Alberto Cafari:** Writing – review & editing, Investigation, Data curation. **Alessandro Cimarello:** Writing – review & editing, Investigation, Data curation. **André Ahlskog:** Writing – review & editing, Investigation, Data curation. **Viljam Grahn:** Writing – review & editing, Investigation, Data curation. **Jari Hyvonen:** Writing – review & editing, Investigation, Data curation.

Declaration of competing interest

The authors declare that they have no known competing financial interests or personal relationships that could have appeared to influence the work reported in this paper.

Appendix. GWP reduction calculation

The calculation of the GWP reduction considers diesel fuel and ammonia as blending fuels, whose properties are reported in Table A1.

Table A1
Properties of the fuels for GWP calculation

Properties	Diesel	Ammonia
Chemical formula	$C_{13.5}H_{23.6}$	NH_3
Lower heating value [MJ/kg]	43.3	18.6

The calculation starts fixing the ammonia energy fraction, y_{NH3}, which allows to quantify energy proportion between diesel and ammonia by Eq. (A1).

$$\begin{cases} E_{NH3} = y_{NH3} E_{tot} \\ E_{die} = (1 - y_{NH3}) E_{tot} \end{cases} \tag{A1}$$

In this equation, E_{tot}, E_{NH3}, and E_{die} are the total fuel energy, the ammonia fuel energy and the diesel fuel energy, respectively. Knowing the chemical formula and the lower heating values of the two fuels, the number of moles of each of those is computed, as reported in Eq. (A2).

$$\begin{cases} n_{NH3} = \dfrac{E_{NH3}}{LHV_{NH3} MW_{NH3}} \\ n_{die} = \dfrac{E_{die}}{LHV_{die} MW_{die}} \end{cases} \tag{A2}$$

In this equation, n_{NH3} and n_{die} represent the moles of ammonia and diesel, respectively, LHV_{NH3} and LHV_{die} denote the corresponding lower heating values, and MW_{NH3} and MW_{die} indicate the corresponding molar weights. At this stage, the chemical composition of an "equivalent" fuel can be computed, considering the mole proportion between diesel and ammonia:

$$n_{die} \cdot (C_{13.5}H_{23.6}) + n_{NH3} \cdot (NH_3) = (n_{die} + n_{NH3}) \cdot (C_x H_y O_z N_f) \tag{A3}$$

Given the equivalent fuel chemical formula, the global chemical reaction of this fuel with air can be solved. In the hypothesis of complete combustion and considering the possibility of lean air/fuel proportions (λ greater than 1), the reaction equation is:

$$\begin{aligned} &C_x H_y O_z N_f + \lambda \left(x + \frac{y}{4} - \frac{z}{2}\right)(O_2 + p_{N2O2} N_2) \rightarrow \\ &x CO_2 + \frac{y}{2} H_2O + p_{N2O2} \left(x + \frac{y}{4} - \frac{z}{2} + \frac{f}{2 \cdot p_{N2O2}}\right) N_2 + \\ &+ (\lambda - 1) \left(x + \frac{y}{4} - \frac{z}{2}\right)(O_2 + p_{N2O2} N_2) \end{aligned} \tag{A4}$$

In this equation, the term p_{N2O2} indicates the nitrogen-to-oxygen molar proportion in the air, assumed equal to 3.733. To consider in the product composition a certain fraction of N_2O, the above reaction is modified also considering as product the molecular hydrogen. This choice does not have any ambition of predicting on chemical kinetics basis the real composition of diesel/ammonia combustion, but only the aim of balancing the atoms counting the reaction. In addition, it is assumed that the combustion occurs in lean conditions (λ equal to 2), typical condition of dual-fuel combustion. With these assumptions, the reaction equation becomes the following:

$$\begin{aligned} &C_x H_y O_z N_f + \lambda \left(x + \frac{y}{4} - \frac{z}{2}\right)(O_2 + p_{N2O2} N_2) \rightarrow \\ &x CO_2 + \left(\frac{y}{2} - k\right) H_2O + k N_2O + k H_2 + p_{N2O2} \left(x + \frac{y}{4} - \frac{z}{2} + \frac{f}{2 \cdot p_{N2O2}} - \frac{k}{p_{N2O2}}\right) N_2 + \\ &+ (\lambda - 1) \left(x + \frac{y}{4} - \frac{z}{2}\right)(O_2 + p_{N2O2} N_2) \end{aligned} \tag{A5}$$

The amount of moles of N_2O (k) is directly derived from the N_2O concentration (p_{N2O}), expressed in ppm:

$$k = \frac{p_{N2O}}{10^6} \cdot n_{prod,tot} \tag{A6}$$

On the basis of the reaction in Eq. (A5) and of the moles of the equivalent fuel, the amount of moles of CO_2 and N_2O and of their mass are computed, in accordance with Eq. (A7):

$$\begin{cases} m_{CO2} = x \cdot (n_{NH3} + n_{die}) \cdot MW_{CO2} \\ m_{N2O} = k \cdot (n_{NH3} + n_{die}) \cdot MW_{N2O} \end{cases} \tag{A7}$$

Known the masses of CO_2 and N_2O, they are converted into equivalent GWP, as reported in Eq. (A8):

$$GWP(y_{amm}, p_{N2O}) = m_{CO2} + 273 \cdot m_{N2O} \tag{A8}$$

These GPW values are in the end compared to the reference condition (pure diesel combustion without N_2O), and the percentage reduction or increase is calculated. The procedure described is repeated from the beginning for different ammonia energy fractions (from 0 to 1) and N_2O concentrations (from 0 to 400 ppm) and the results are collected in Fig. 1.

References

[1] Reitz RD, Ogawa H, Payri R, Fansler T, Kokjohn S, Moriyoshi Y, et al. IJER editorial: the future of the internal combustion engine. Int J Engine Res 2020;21:3–10. https://doi.org/10.1177/1468087419877990.

[2] United Nations. Sustainable Development Goal 13: take urgent action to combat climate change and its impacts. 2020.

[3] Commission E, for Climate Action D-G, for Energy D-G, for Mobility D-G, Transport, De Vita A, et al. EU reference scenario 2020 – energy, transport and GHG emissions – trends to 2050. Publications Office; 2021. https://doi.org/10.2833/35750.

[4] Andersson Ö, Börjesson P. The greenhouse gas emissions of an electrified vehicle combined with renewable fuels: life cycle assessment and policy implications. Appl Energy 2021;289:116621. https://doi.org/10.1016/j.apenergy.2021.116621.

[5] Gl DNV, Safer S, Dnv G. Maritime forecast to 2050. Energy Transition Outlook 2018;1:1–117.

[6] Joung T-H, Kang S-G, Lee J-K, Ahn J. The IMO initial strategy for reducing Greenhouse Gas(GHG) emissions, and its follow-up actions towards 2050. Journal of International Maritime Safety, Environmental Affairs, and Shipping 2020;4:1–7. https://doi.org/10.1080/25725084.2019.1707938.

[7] Bushiri D. Comparing green fuels for marine engines - part 1. Hydrocarbon Processing Magazine n.d. https://www.hydrocarbonprocessing.com/magazine/2022/january-2022/biofuels-alternativerenewable-fuels/comparing-green-fuelsfor-marine-engines-part-1. [Accessed 30 January 2025].

[8] Brynolf S, Fridell E, Andersson K. Environmental assessment of marine fuels: liquefied natural gas, liquefied biogas, methanol and bio-methanol. J Clean Prod 2014;74:86–95. https://doi.org/10.1016/j.jclepro.2014.03.052.

[9] Brynolf S, Hansson J, Anderson JE, Skov IR, Wallington TJ, Grahn M, et al. Review of electrofuel feasibility—prospects for road, ocean, and air transport. Progress in Energy 2022;4:042007. https://doi.org/10.1088/2516-1083/ac8097.

[10] Curran S, Onorati A, Payri R, Agarwal AK, Arcoumanis C, Bae C, et al. The future of ship engines: renewable fuels and enabling technologies for decarbonization. Int J Engine Res 2024;25:85–110. https://doi.org/10.1177/14680874231187954.

[11] Shi J, Zhu Y, Feng Y, Yang J, Xia C. A prompt decarbonization pathway for shipping: green hydrogen, ammonia, and methanol production and utilization in marine engines. Atmosphere 2023;14:584. https://doi.org/10.3390/atmos14030584.

[12] Gil Posada JO, Abdalla AH, Oseghale CI, Hall PJ. Multiple regression analysis in the development of NiFe cells as energy storage solutions for intermittent power sources such as wind or solar. Int J Hydrogen Energy 2016;41:16330–7. https://doi.org/10.1016/j.ijhydene.2016.04.165.

[13] Science and Technology Promotion Agency Public Relations Division. Establishment of "green ammonia consortium". JST 2017;1:1. https://www.jst.go.jp/osirase/20170725/index.html [Accessed 31 January 2025].

[14] Brown T. Industrial demonstrations of ammonia fuel in Japan. Ammonia Energy 2017;1:1. https://ammoniaindustry.com/industrial-demonstrations-of-ammonia-fuel-in-japan/ [Accessed 31 January 2025].

[15] Crolius S. REFUEL is back on track. Ammonia Energy 2017. http://www.ammoniaenergy.org/refuel-is-back-on-track/2017. [Accessed 31 January 2025].

[16] Crolius S. U of MN's ammonia program. UMN 2016;1:1. https://wcroc.cfans.umn.edu/news/ammonia-program [Accessed 31 January 2025].

[17] SIEMENS. Green decoupled ammonia supply. Siemens 2017;1:1. https://www.siemens.co.uk/en/insights/potential-of-green-ammonia-as-fertiliser-and-electricity-storage.htm [Accessed 31 January 2025].

[18] Howell D. Revolutionary disruption coming to the energy sector. Jpn Times 2017;1:1. https://www.japantimes.co.jp/opinion/2017/03/10/commentary/world-commentary/revolutionary-disruption-coming-energy-sector [Accessed 31 January 2025].

[19] Crolius S. NH3 fuel association chapter launching in Australia. Ammonia Energy 2017. http://www.ammoniaenergy.org/nh3-fuel-association-chapter-launching-in-australia/. [Accessed 31 January 2025].

[20] Vries ND. Ammonia: from kitchen-and-garden means to fuel for ships? Pioneer Ship 2040. C-Job; 2017.

[21] International Energy Agency. Energy technology perspectives. 2017.

[22] Corporation Wartsila. Wärtsilä continues to set the pace for marine decarbonisation with launch of world-first 4-stroke engine-based ammonia solution 2023. https://www.wartsila.com/media/news/15-11-2023-wartsila-continues-to-set-the-pace-for-marine-decarbonisation-with-launch-of-world-first-4-stroke-engine-based-ammonia-solution-3357985. [Accessed 31 January 2025].

[23] Pedersen KA, Lewandowski MT, Bjørgen KOP, Løvås T. Identification of N2O formation in an ammonia/n-heptane dual-fueled compression ignition engine using numerical simulations. Fuel 2025;381:133556. https://doi.org/10.1016/j.fuel.2024.133556.

[24] Bjørgen KOP, Emberson DR, Løvås T. Combustion of liquid ammonia and diesel in a compression ignition engine operated in high-pressure dual fuel mode. Fuel 2024;360:130269. https://doi.org/10.1016/j.fuel.2023.130269.

[25] Nadimi E, Przybyła G, Lewandowski MT, Adamczyk W. Effects of ammonia on combustion, emissions, and performance of the ammonia/diesel dual-fuel compression ignition engine. J Energy Inst 2023;107:101158. https://doi.org/10.1016/j.joei.2022.101158.

[26] Ichikawa Y, Niki Y, Takasaki K, Kobayashi H, Miyanagi A. NH3 combustion using three-layer stratified fuel injection for a large two-stroke marine engine: experimental verification of the concept. Applications in Energy and Combustion Science 2022;10:100071. https://doi.org/10.1016/j.jaecs.2022.100071.

[27] Yousefi A, Guo H, Dev S, Liko B, Lafrance S. Effects of ammonia energy fraction and diesel injection timing on combustion and emissions of an ammonia/diesel dual-fuel engine. Fuel 2022;314:122723. https://doi.org/10.1016/j.fuel.2021.122723.

[28] The Earth's Energy Budget. Climate feedbacks and climate sensitivity. Climate change 2021 – the physical science basis. Cambridge University Press; 2023. p. 923–1054. https://doi.org/10.1017/9781009157896.009.

[29] Reiter AJ, Kong S-C. Combustion and emissions characteristics of compression-ignition engine using dual ammonia-diesel fuel. Fuel 2011;90:87–97. https://doi.org/10.1016/j.fuel.2010.07.055.

[30] Ryu K, Zacharakis-Jutz GE, Kong S-C. Performance characteristics of compression-ignition engine using high concentration of ammonia mixed with dimethyl ether. Appl Energy 2014;113:488–99. https://doi.org/10.1016/j.apenergy.2013.07.065.

[31] Dupuy A, de Castro R, Bréquigny P, Mounaïm-Rousselle C. Comparison of combustion process of ammonia internal combustion engine: premixed and RCCI combustion. European Combustion Meeting 2023;14. Rouen (FR), France.

[32] Kokjohn SL, Hanson RM, Splitter DA, Reitz RD. Fuel reactivity controlled compression ignition (RCCI): a pathway to controlled high-efficiency clean combustion. Int J Engine Res 2011;12:209–26. https://doi.org/10.1177/1468087411401548.

[33] Valera-Medina A, Xiao H, Owen-Jones M, David WIF, Bowen PJ. Ammonia for power. Prog Energy Combust Sci 2018;69:63–102. https://doi.org/10.1016/j.pecs.2018.07.001.

[34] Chiera D, Wood J, Jones A, Buehner M, Polley N, Hampson GJ. Method to reach high substitution of an ammonia fueled engine using dual fuel RCCI and active combustion control. ASME 2022 ICE Forward Conference. American Society of Mechanical Engineers; 2022. https://doi.org/10.1115/ICEF2022-88759.

[35] Kumar D, Valera H, Agarwal AK. Numerical predictions of In-Cylinder phenomenon in methanol fueled locomotive engine using high pressure direct injection technique. https://doi.org/10.4271/2021-01-0492; 2021.

[36] Payri R, Bracho G, Martí-Aldaraví P, Marco-Gimeno J. Numerical analysis of urea to ammonia conversion in automotive selective catalytic reduction realistic conditions. Ind Eng Chem Res 2021;60:14329–40. https://doi.org/10.1021/acs.iecr.1c02627.

[37] Dupuy A, Brequigny P, Schmid A, Frapolli N, Mounaïm-Rousselle C. Experimental study of RCCI engine -Ammonia combustion with diesel pilot injection. Journal of Ammonia Energy 2023;1. https://doi.org/10.18573/jae.6.

[38] Dahham RY, Zhang R, Pan J, Mao X, Wei H, Li W. Combustion and Emission Characteristics of *n* -Heptane/NH_3 at RCCI Mode: emphasis on an Injection Strategy. Energy & Fuels 2024;38:14730–42. https://doi.org/10.1021/acs.energyfuels.4c01654.

[39] Hossein Fakhari A, Gharehghani A, Mahdi Salahi M, Mahmoudzadeh Andwari A. RCCI combustion of ammonia in dual fuel engine with early injection of diesel fuel. Fuel 2024;365:131182. https://doi.org/10.1016/j.fuel.2024.131182.

[40] Fakhari AH, Gharehghani A, Salahi MM, Andwari AM. Numerical investigation of the hydrogen-enriched ammonia-diesel RCCI combustion engine. Fuel 2024;375:132579. https://doi.org/10.1016/j.fuel.2024.132579.

[41] Vasudev A, Mikulski M, Balakrishnan PR, Storm X, Hunicz J. Thermo-kinetic multi-zone modelling of low temperature combustion engines. Prog Energy Combust Sci 2022;91:100998. https://doi.org/10.1016/j.pecs.2022.100998.

[42] De Bellis V, Malfi E, Lanotte A, Fasulo G, Bozza F, Cafari A, et al. Development of a phenomenological model for the description of RCCI combustion in a dual-fuel marine internal combustion engine. Appl Energy 2022;325:119919. https://doi.org/10.1016/j.apenergy.2022.119919.

[43] De Felice M, De Bellis V, Malfi E, Gambardella A, Bozza F, Cafari A, et al. A novel phenomenological model for stratification-controlled low temperature combustion applied to a dual-fuel marine internal combustion engine supplied with natural gas and light fuel oil. Fuel 2025;386:134218. https://doi.org/10.1016/j.fuel.2024.134218.

[44] Kokjohn SL, Hanson RM, Splitter DA, Reitz RD. Experiments and modeling of dual-fuel HCCI and PCCI combustion using In-Cylinder fuel blending. SAE Int J Engines 2009;2:24–39. https://doi.org/10.4271/2009-01-2647.

[45] Benajes J, Molina S, García A, Belarte E, Vanvolsem M. An investigation on RCCI combustion in a heavy duty diesel engine using in-cylinder blending of diesel and gasoline fuels. Appl Therm Eng 2014;63:66–76. https://doi.org/10.1016/j.applthermaleng.2013.10.052.

[46] Yang W, Zhou D, Zhao F, Li J. Dual fuel RCCI engine combustion modeling with detailed chemistry considering flame propagation in partially premixed combustion. Appl Energy 2017;203:164–76. https://doi.org/10.1016/j.apenergy.2017.06.021.

[47] Belaid-Saleh H, Jay S, Kashdan J, Ternel C, Mounaïm-Rousselle C. Numerical and experimental investigation of combustion regimes in a dual fuel engine. https://doi.org/10.4271/2013-24-0015; 2013.

[48] Rostampour A, Shojaeefard MH, Molaeimanesh GR. Investigation of flame propagation and pollutants Formation within a combustion chamber of an RCCI engine. Iranian Journal of Science and Technology, Transactions of Mechanical Engineering 2023;47:345–61. https://doi.org/10.1007/s40997-022-00504-1.

[49] Cheng C, Cordtz RF, Førby NL, Schramm J. Experimental and simulation investigation of n-heptane/ammonia dual fuel on a light-duty compression ignition engine. Int J Hydrogen Energy 2024;57:1339–53. https://doi.org/10.1016/j.ijhydene.2024.01.130.

[50] Al-Dawody MF, Al-Obaidi W, Aboud ED, Abdulwahid MA, Al-Farhany K, Jamshed W, et al. Mechanical engineering advantages of a dual fuel diesel engine powered by diesel and aqueous ammonia blends. Fuel 2023;346:128398. https://doi.org/10.1016/j.fuel.2023.128398.

[51] Martz JB, Middleton RJ, Lavoie GA, Babajimopoulos A, Assanis DN. A computational study and correlation of premixed isooctane–air laminar reaction front properties under spark ignited and spark assisted compression ignition engine conditions. Combust Flame 2011;158:1089–96. https://doi.org/10.1016/j.combustflame.2010.09.014.
[52] Martz JB, Lavoie GA, Im HG, Middleton RJ, Babajimopoulos A, Assanis DN. The propagation of a laminar reaction front during end-gas auto-ignition. Combust Flame 2012;159:2077–86. https://doi.org/10.1016/j.combustflame.2012.01.011.
[53] Babajimopoulos A, Assanis DN, Flowers DL, Aceves SM, Hessel RP. A fully coupled computational fluid dynamics and multi-zone model with detailed chemical kinetics for the simulation of premixed charge compression ignition engines. Int J Engine Res 2005;6:497–512. https://doi.org/10.1243/146808705X30503.
[54] Hockett A, Hampson G, Marchese AJ. Development and validation of a reduced chemical kinetic mechanism for computational fluid dynamics simulations of natural gas/diesel dual-fuel engines. Energy & Fuels 2016;30:2414–27. https://doi.org/10.1021/acs.energyfuels.5b02655.
[55] Fiveland S, Assanis D. Development of a two-zone HCCI combustion model accounting for boundary layer effects. SAE Technical Paper 2001. https://doi.org/10.4271/2001-01-1028.
[56] Noda T, Foster D. A numerical Study to control combustion duration of hydrogen-fueled HCCI by using multi-zone Chemical Kinetics Simulation. SAE Technical Paper 2001. https://doi.org/10.4271/2001-01-0250.
[57] Zhou Y, Gainey B, Lawler B. An ultrafast multi-zone HCCI model with Autoignition, global reaction and Interpolation (AGI) for achieving comparable accuracy to detailed chemical kinetics models. Combust Flame 2020;221:487–501. https://doi.org/10.1016/j.combustflame.2020.08.016.
[58] Livengood JC, Wu PC. Correlation of autoignition phenomena in internal combustion engines and rapid compression machines. Symposium (International) on Combustion 1955;5:347–56. https://doi.org/10.1016/S0082-0784(55)80047-1.
[59] Park J-W, Jouzdani S, Tzanetakis T, Schmidt H, Atkinson W, Naber J, et al. Experimental diesel spray characterization of the medium-duty injector with single- and multi-hole nozzle configurations under non-reacting, non-vaporizing conditions. Front Mech Eng 2022;8. https://doi.org/10.3389/fmech.2022.931377.
[60] Benajes J, Pastor JV, García A, Monsalve-Serrano J. The potential of RCCI concept to meet EURO VI NOx limitation and ultra-low soot emissions in a heavy-duty engine over the whole engine map. Fuel 2015;159:952–61. https://doi.org/10.1016/j.fuel.2015.07.064.
[61] Pastor J, Javier Lopez J, Garcia J, Pastor J. A 1D model for the description of mixing-controlled inert diesel sprays. Fuel 2008;87:2871–85. https://doi.org/10.1016/j.fuel.2008.04.017.
[62] Musculus M, Kattke K. Entrainment waves in diesel jets. SAE Int J Engines 2009;2:1170–93. https://doi.org/10.4271/2009-01-1355.
[63] Nazemi M, Shahbakhti M. Modeling and analysis of fuel injection parameters for combustion and performance of an RCCI engine. Appl Energy 2016;165:135–50. https://doi.org/10.1016/j.apenergy.2015.11.093.
[64] Bekdemir C, Baert R, Willems F, Somers B. Towards control-oriented modeling of natural gas-diesel RCCI combustion. SAE Technical Paper 2015. https://doi.org/10.4271/2015-01-1745.
[65] Bhagatwala A, Sankaran R, Kokjohn S, Chen J-Y. Numerical investigation of spontaneous flame propagation under RCCI conditions. Combust Flame 2015;162:3412–26. https://doi.org/10.1016/j.combustflame.2015.06.005.
[66] Roberts G, Rousselle CM, Musculus M, Wissink M, Curran S, Eagle E. RCCI combustion regime transitions in a single-cylinder optical engine and a multi-cylinder metal engine. SAE Int J Engines 2017;10:2392–413. https://doi.org/10.4271/2017-24-0088.
[67] Karimkashi S, Kahila H, Kaario O, Larmi M, Vuorinen V. A numerical study on combustion mode characterization for locally stratified dual-fuel mixtures. Combust Flame 2020;214:121–35. https://doi.org/10.1016/j.combustflame.2019.12.030.
[68] Komninos NP, Kosmadakis GM. Heat transfer in HCCI multi-zone modeling: validation of a new wall heat flux correlation under motoring conditions. Appl Energy 2011;88:1635–48. https://doi.org/10.1016/j.apenergy.2010.11.039.
[69] Pickett LM, Manin J, Genzale CL, Siebers DL, Musculus MPB, Idicheria CA. Relationship between diesel fuel Spray Vapor Penetration/Dispersion and local fuel mixture fraction. SAE Int J Engines 2011;4. https://doi.org/10.4271/2011-01-0686. 2011-01–0686.
[70] Singh S, Musculus MPB. Numerical modeling and analysis of entrainment in turbulent jets after the end of injection. J Fluid Eng 2010;132. https://doi.org/10.1115/1.4002184.
[71] Arai M, Tabata M, Hiroyasu H, Shimizu M. Disintegrating process and spray characterization of fuel jet injected by a diesel nozzle. https://doi.org/10.4271/840275; 1984.
[72] Hiroyasu H, Arai M. Structures of fuel sprays in diesel engines. https://doi.org/10.4271/900475; 1990.
[73] Arrègle J, Pastor JV, Ruiz S. The influence of injection parameters on diesel spray characteristics. https://doi.org/10.4271/1999-01-0200; 1999.
[74] Delacourt E, Desmet B, Besson B. Characterisation of very high pressure diesel sprays using digital imaging techniques. Fuel 2005;84:859–67. https://doi.org/10.1016/j.fuel.2004.12.003.
[75] Andreassi L, Ubertini S, Allocca L. Experimental and numerical analysis of high pressure diesel spray–wall interaction. Int J Multiphas Flow 2007;33:742–65. https://doi.org/10.1016/j.ijmultiphaseflow.2007.01.003.
[76] Abramzon B, Sirignano WA. Droplet vaporization model for spray combustion calculations. Int J Heat Mass Tran 1989;32:1605–18. https://doi.org/10.1016/0017-9310(89)90043-4.
[77] Yuen MC, Chen LW. On drag of evaporating liquid droplets. Combust Sci Technol 1976;14:147–54. https://doi.org/10.1080/00102207608547524.
[78] Morel T, Wahiduzzaman S. Modeling of diesel combustion and emissions. XXVI FISITA Congress 1996.
[79] Zhang Y, Jia M, Yi P, Liu H, Xie M. An efficient liquid film vaporization model for multi-component fuels considering thermal and mass diffusions. Appl Therm Eng 2017;112:534–48. https://doi.org/10.1016/j.applthermaleng.2016.10.046.
[80] Woschni G. A universally applicable equation for the instantaneous heat transfer coefficient in the internal combustion engine. SAE Technical Paper 1967. https://doi.org/10.4271/670931.
[81] Kodavasal J, McNenly MJ, Babajimopoulos A, Aceves SM, Assanis DN, Havstad MA, et al. An accelerated multi-zone model for engine cycle simulation of homogeneous charge compression ignition combustion. Int J Engine Res 2013;14:416–33. https://doi.org/10.1177/1468087413482480.
[82] Kong SC, Reitz RD. Use of detailed chemical kinetics to study HCCI engine combustion with consideration of turbulent mixing effects. J Eng Gas Turbines Power 2002;124:702–7. https://doi.org/10.1115/1.1413766.
[83] De Bellis V, Malfi E, Lanotte A, De Felice M, Teodosio L, Bozza F. A tabulated chemistry multi-zone combustion model of HCCI engines supplied with pure fuel and fuel blends. Energies 2022;16:265. https://doi.org/10.3390/en16010265.
[84] De Bellis V, Malfi E, Lanotte A, Fasulo G, Bozza F. A multi-zone combustion model integrated with a fast tabulated chemical kinetics applied for the simulation of HCCI engines supplied with hydrogen or carbon-based fuels. https://doi.org/10.4271/2022-01-0388; 2022.
[85] Bozza F, De Bellis V, Teodosio L. A tabulated-chemistry approach applied to a quasi-dimensional combustion model for a fast and accurate knock prediction in spark-ignition engines. https://doi.org/10.4271/2019-01-0471; 2019.
[86] Xu S, Li G, Zhou M, Yu W, Zhang Z, Hou D, et al. Experimental and kinetic studies of extinction limits of counterflow cool and hot diffusion flames of ammonia/n-dodecane. Combust Flame 2022;245:112316. https://doi.org/10.1016/j.combustflame.2022.112316.
[87] Kim N, Guahk YT. Numerical modeling for local flame structure and pollutant formation in biodiesel and n-Dodecane spray jet flames. Fuel 2022;321:124151. https://doi.org/10.1016/j.fuel.2022.124151.
[88] Kannan J, Gadalla M, Tekgül B, Karimkashi S, Kaario O, Vuorinen V. Large eddy simulation of diesel spray–assisted dual-fuel ignition: a comparative study on two *n* -dodecane mechanisms at different ambient temperatures. Int J Engine Res 2021;22:2521–32. https://doi.org/10.1177/1468087420946551.
[89] Som S, Longman DE, Luo Z, Plomer M, Lu T. Three dimensional simulations of diesel sprays using n-dodecane as a surrogate. Fall technical meeting of the eastern states section of the combustion institute 2011;12.
[90] Verhelst S, Sheppard CGW. Multi-zone thermodynamic modelling of spark-ignition engine combustion—an overview. Energy Convers Manag 2009;50:1326–35. https://doi.org/10.1016/j.enconman.2009.01.002.
[91] Gouldin FC. An application of fractals to modeling premixed turbulent flames. Combust Flame 1987;68:249–66. https://doi.org/10.1016/0010-2180(87)90003-4.
[92] De Bellis V, Severi E, Fontanesi S, Bozza F. Hierarchical 1D/3D approach for the development of a turbulent combustion model applied to a VVA turbocharged engine. Part II: combustion model. Energy Proc 2014;45:1027–36. https://doi.org/10.1016/j.egypro.2014.01.108.
[93] De Bellis V, Bozza F, Tufano D. A comparison between two phenomenological combustion models applied to different SI engines. https://doi.org/10.4271/2017-01-2184; 2017.
[94] Goldmann A, Dinkelacker F. Approximation of laminar flame characteristics on premixed ammonia/hydrogen/nitrogen/air mixtures at elevated temperatures and pressures. Fuel 2018;224:366–78. https://doi.org/10.1016/j.fuel.2018.03.030.
[95] D'Adamo A, Del Pecchia M, Breda S, Berni F, Fontanesi S, Prager J. Chemistry-based laminar flame speed correlations for a wide range of engine conditions for iso-octane, n-heptane, toluene, and gasoline surrogate fuels. SAE 2017 International Powertrains, Fuels and Lubricants Meeting, FFL 2017, SAE International 2017. https://doi.org/10.4271/2017-01-2190.
[96] Bozza F, Berni F, Cicci F, D'Adamo A, De Bellis V, Fontanesi S, et al. Potentials of the oversizing and H2-Supported lean combustion of a VVA SI gasoline engine towards efficiency improvement. In: SAE 15th international conference on engines and vehicles, ICE, vol. 1. SAE International; 2021, 2021. https://doi.org/10.4271/2021-24-0007.
[97] Bhat V, Tamma BK. Development of multi-zone phenomenological model for SI engine. SAE Technical Paper 2014. https://doi.org/10.4271/2014-01-1068.
[98] Lavoie GA, Heywood JB, Keck JC. Experimental and theoretical Study of nitric oxide Formation in internal combustion engines. Combust Sci Technol 1970;1:313–26. https://doi.org/10.1080/00102206908952211.
[99] Tornatore C, Marchitto L, Sabia P, De Joannon M. Ammonia as green fuel in internal combustion engines: State-of-the-Art and future perspectives. Front Mech Eng 2022;8. https://doi.org/10.3389/fmech.2022.944201.
[100] Tutak W. Co-combustion of ammonia and hydrogen in spark ignition engines - state-of-the-art and challenges. Int J Hydrogen Energy 2024;80:188–205. https://doi.org/10.1016/j.ijhydene.2024.07.163.
[101] Elbaz AM, Wang S, Guiberti TF, Roberts WL. Review on the recent advances on ammonia combustion from the fundamentals to the applications. Fuel Communications 2022;10:100053. https://doi.org/10.1016/j.jfueco.2022.100053.

[102] De Bellis V, Malfi E, De Felice M, Lanotte A, Cafari A, Caputo G, et al. A comprehensive phenomenological model for unburned fuel emission simulation applied to natural gas engines. Fuel 2024;367:131440. https://doi.org/10.1016/j.fuel.2024.131440.

[103] Malfi E, Esposito S, De Felice M, Pitsch H, Pischinger S, De Bellis V. Phenomenological model for unburned hydrocarbon emissions from spark-ignition, pre-chamber, and dual-fuel internal combustion engines. Int J Engine Res 2024;25:1818–34. https://doi.org/10.1177/14680874241255157.

[104] Suckart D, Linse D, Schutting E, Eichlseder H. Experimental and simulative investigation of flame–wall interactions and quenching in spark-ignition engines. Automotive and Engine Technology 2017;2:25–38. https://doi.org/10.1007/s41104-016-0015-z.

[105] Westbrook CK, Dryer FL. Simplified reaction mechanisms for the oxidation of hydrocarbon fuels in flames. Combust Sci Technol 1981;27:31–43. https://doi.org/10.1080/00102208108946970.